Catalysis Letters (2026) 156:192
https://doi.org/10.1007/s10562-026-05415-3

Transformation of α-Pinene and Limonene Over Water Treatment Sludge-Derived Catalysts

Mateo Moreno Giraldo[1] · **Aída Luz Villa**[1]

Received: 11 March 2026 / Accepted: 15 May 2026

Abstract

The mud provided by the process of purification of water contains metals such as aluminum, silicon and iron which have significant potential for catalytic applications. Sludge after thermal (LS600) and chemical treatment with HCl (LS600-HCl) and subsequently with iron (LS600-HCl-Fe7%) were used as catalysts in the transformation of α-pinene and limonene. The thermal treatment removed organic matter and concentrated the metal oxides, while the HCl treatment improved the acidity that was enhanced with the addition of iron. The LS600-HCl catalyst favored the isomerization of α-pinene with 85% conversion and 39% selectivity towards camphene, while over LS600-HCl-Fe7% catalyst, complete conversion of limonene was reached with 44% selectivity towards *p*-cymene. The treated materials showed increases in acidic sites, with Lewis acidity associated with metals such as Al and Fe. LS600-HCl and LS600-HCl-Fe7% materials had surface areas of 103 and 84 m^2/g, respectively, dominated by mesopores, with slight morphological changes but greater roughness. Mössbauer analysis of the LS600-HCl-Fe7% material showed 36% magnetite and maghemite, and 64% paramagnetic phases such as hematite or goethite.

✉ Mateo Moreno Giraldo
mateo.moreno1@udea.edu.co

Aída Luz Villa
aida.villa@udea.edu.co

[1] Environmental Catalysis Research Group, Department of Chemical Engineering, Faculty of Engineering, Universidad de Antioquia UdeA, Medellín, Colombia

Published online: 12 June 2026

Graphical Abstract

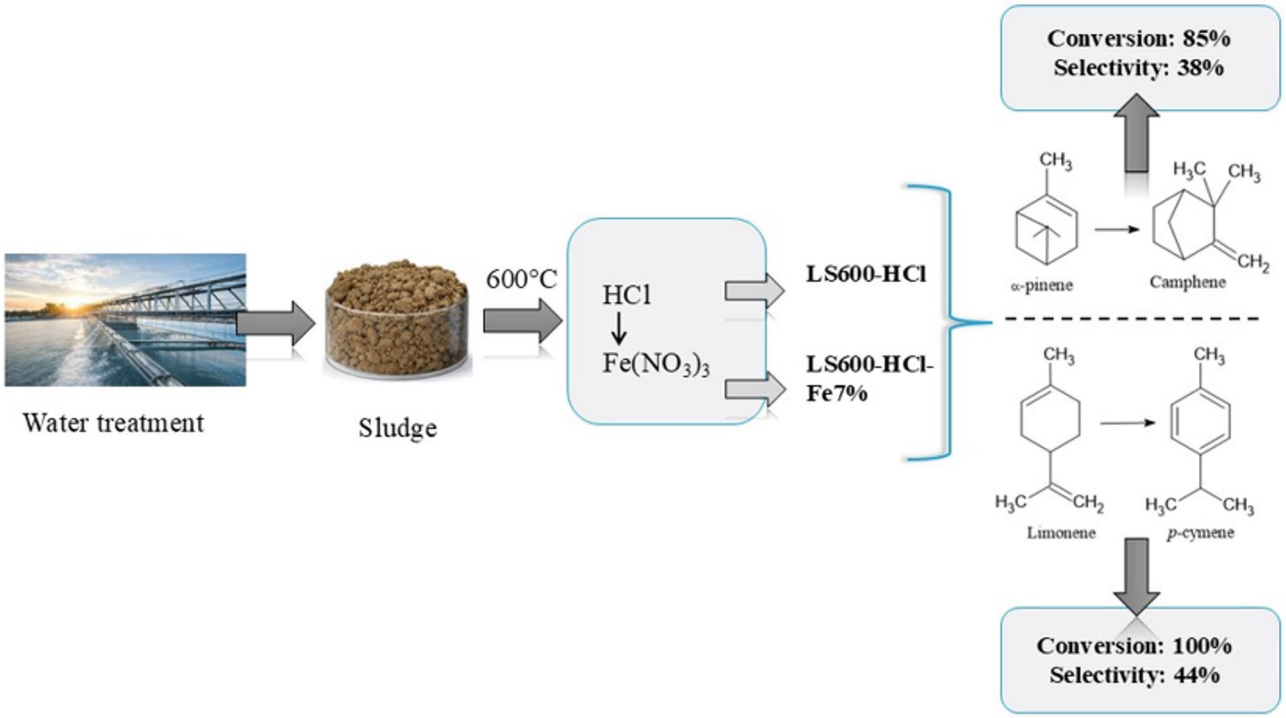

Keywords Heterogeneous catalysts · α-pinene · Camphene · Limonene · *p*-cymene

Abbreviations

A	Anortithe
A_i	Initial GC area
Al	Albite
An	Amphibole
A_p	GC area of reaction products
A_s	GC area of limonene
A_t	GC area at reaction time
B	Brønsted acid sites
BET	Brunauer–Emmett–Teller
BJH	Barrett–Joyner–Halenda
C	α-quartz
CLIN	Clinoptilolite
d_p	Pore diameter
DRIFTS	Diffuse reflectance infrared Fourier transform Spectroscopy
FID	Flame ionization detector
FTIR-Py	Fourier transform infrared spectroscopy of adsorbed pyridine
GC-MS	Gas chromatography–mass spectrometry
H	Hematite
IUPAC	International union of pure and applied chemistry
L	Lewis acid sites
LS	Sludge from a water treatment plant
LS600	Thermally treated sludge
LS600-HCl	Sludge treated thermally and with HCl
LS600-HCl-Fe7%	Sludge treated thermally, with HCl and Fe
LS600-HCl-R	Sludge treated thermally and with reused HCl
M	Magnetite
Mh	Maghemite
NH_3-TPD	Ammonia temperature-programmed desorption
SBL	Sludge-based support of the metallic active phase
SEM	Scanning electron microscopy
S_j	Selectivity for the product of interest
TCD	Thermal Conductivity Detector
TGA	Thermogravimetric analysis
V_p	Total pore volume
X	Conversion of substrate
XRD	X-ray diffraction
XRF	X-ray fluorescence

1 Introduction

With continuous population growth, the amount of waste generated during water purification processes also increases [1]. In the coagulation-flocculation step, coagulants such as aluminum sulfate or ferric salts destabilize colloidal matter and generate suspended solids that are subsequently removed by sedimentation and filtration, producing drinking water treatment sludge [2, 3]. This sludge contains large amounts of water as well as organic and inorganic components that pose environmental and public-health concerns. Current disposal routes (landfilling, discharge, agricultural application, incineration) have significant operational costs and environmental impacts [4, 5]. A promising alternative valorization route is to use the inorganic fraction of the sludge, which is rich in Al, Si, Ti, and Fe, as a precursor for heterogeneous catalysts applicable to a variety of reactions, including the transformation of terpenes into higher value-added products [6–8].

α-Pinene and limonene, major components of turpentine and citrus essential oils, respectively, can be isomerized and/or dehydrogenated over acid and bifunctional catalysts to yield camphene (used as a precursor for resins, flavors, fragrances, pharmaceuticals, and fuels) and *p*-cymene (used as an intermediate in the synthesis of fine chemicals, terephthalic acid, thymol, carvacrol, and as a ligand in metathesis catalysts) [8, 16]. Both reactions proceed through carbocationic intermediates that form upon protonation of the C = C bond by Brønsted acid sites and rearrange to the target products. For limonene to *p*-cymene, an additional dehydrogenation step is required, which is typically promoted by metal or metal-oxide sites.

A wide range of heterogeneous catalysts has been reported for these transformations. For α-pinene isomerization to camphene, active systems include acid-modified natural zeolites (clinoptilolite, mordenite, ferrierite), TiO_2-based materials, mesoporous Ti-SBA-15, molybdenum-titanium mixed oxides, biomass-derived activated carbons, montmorillonites, and sulfonated carbon acids [6–15]. Reported camphene selectivities typically fall in the 27–69% range at substrate conversions of 40–100%, under temperatures between 70 and 180 °C. A quantitative comparison of the most relevant systems is given in Table 1. For limonene to *p*-cymene, effective catalysts include acid-activated mordenite and montmorillonite, supported noble metals (Pd, Pt, Ni) on alumina, sepiolite modified with Fe or Mn under microwave irradiation, mixed silica–alumina oxides, Ti-MCM-41, supported heteropolyacids, and CdO/SiO_2 systems [16–23]. Reported *p*-cymene selectivities span 45–100% at 140–250 °C, as summarized in Table 2. In general, high selectivities are achieved either under severe conditions (T ≥ 200 °C, gas phase) or with expensive synthetic supports (mesoporous silicates, noble metals on alumina).

Against this background, there is a clear opportunity to investigate low-cost, waste-derived precursors as alternatives to conventional catalysts. In this work, drinking water treatment sludge from a purification plant located in western Medellín (Colombia) was characterized and subjected

Table 1 Literature reports on the synthesis of camphene from α-pinene

Catalyst (g)	α-Pinene (mmol)	Solvent (mL)	T (°C)	t (h)	Conversion (%)	Camphene selectivity (%)	References
CLIN 0.1 (2.00)	140.0	NR	70	0.06	100	50	[8]
0.7Fe-CL[a] (0.30)	13.0	NR	155	8	94	66	[6]
H-Z1 (0.25)	31.0	NR	75	3	40	51	[9]
TiO_2 (0.60)	629.0	NR	155	0.67	100	69	[7]
Ti-SBA-15 (0.60)	29.0	NR	180	7	100	27	[10]
NT-TiO_2 (0.05)	0.25	Cyclohexane (3)	90	1	21	50	[11]
AcMo (0.05)	0.25	Cyclohexane (3)	90	1	NR	48	
MoO_3 (0.05)	0.25	Cyclohexane (3)	90	1	NR	29	
AcMo/P-25 (0.05)	0.25	Cyclohexane (3)	90	1	21	41	
TiO_2-acetic acid (0.8)	628.0	NR	155	1.75	100	68	[12]
AC_SH_H_3PO_4 (0.15)	18.0	NR	160	3	50	57	[13]
AC_OP_H_3PO_4 (0.15)	18.0	NR	160	3	47	53	
AC_SCG_H_3PO_4 (0.15)	18.0	NR	160	3	13	55	
Al (0.5)	0.59	NR	140	6	35	52	[14]
AC_{400-3}-$P_{1.5}$-SO_3H_{180-8} (0.05)	22.0	NR	110	10	99	51	[15]

Nitrogen atmosphere

NR not reported, *CLIN 0.1* Clinoptilolite treated with 0.1 M H2SO4, *0.7Fe−CL* Clinoptilolite treated with 0.7 ppm iron, *H−Z1* de−aluminated ferrierite−type zeolite, *Ti−SBA−15* SBA−15 material treated with titanium, *NT−TiO2* titanium nanotubes, *AcMo* molybdic acid, *AcMo/P−25* titanium−based molybdic acid, *AC_SH* activated carbon from sunflower husks, *AC_OP* activated carbon from orange peels, *AC_SCG* activated carbon from ground coffee, *Al 0.5* 30% montmorillonite, 0.5% of Al, AC400−3−P1.5−SO3H180−8 0.05 carbon−based acid by sulfonating activated carbon derived from eucalyptus wood waste

Table 2 Literature reports on the synthesis of *p*-cymene from limonene

Catalyst (g)	Limonene (mmol)	Solvent (mL)	T (°C)	t (h)	Conversion (%)	*p*-Cymene selectivity (%)	Reference
Technosa-S_2 (1.00)	113	Tetraethylene glycol dimethyl ether (15)	140	7.0	NR	60	[17]
Pd/Al_2O_3	NR	Ethanol, 2-propanol*	350	0.01	100	45	[18]
Sepiolita-Fe** (0.50)	31	NR	110	0.3	100	88	[19]
Sepiolita-Mn** (0.50)	31	NR	110	0.3	100	77	
M_2-9 h (1.00)	113	Tetraethylene glycol dimethyl ether (15)	140	9.0	100	75	[20]
SIRAL 40** (0.50)	31	NR	165	0.3	100	100	[16]
Ti-MCM-41 (0.75)	37	NR	170	24.0	96	46	[21]
20%CdO/SiO_2*** (0.20)	NR	NR	250	4.0	100	100	[23]

NR not reported

*Supercritical alcohols

Technosa−S2: natural mordenite treated with H2SO4. M2–9 h: natural montmorillonite treated with HCl and with a reaction time of 9 h. SIRAL 40: mixed oxide of alumina and silica with 40% silica. **Use of microwaves. ***Gas phase

to thermal and chemical treatments (calcination, HCl treatment, and Fe impregnation), and the resulting materials were evaluated as catalysts for the isomerization of α-pinene to camphene and the isomerization/dehydrogenation of limonene to *p*-cymene. The novelty of the study lies in using an industrial waste stream rather than a synthetic precursor as a source of active catalytic materials, and in showing that modest but meaningful selectivities to the target products can be obtained under mild conditions.

2 Experimental Section

2.1 Materials

Sludge supplied by Empresas Públicas de Medellín (EPM) was used, obtained from the tailings of a water purification plant (LS) located in the west of the city of Medellín, Antioquia [2]. α-Pinene (98%, Sigma-Aldrich 98%), cyclohexane (99.5%, Mallinckrodt Chemical), (R)(+) limonene (97% Sigma-Aldrich), hydrochloric acid (37%, Merck), and iron (III) nitrate nonahydrate ($Fe(NO_3)_3.9H_2O$, Merck) were used without further purification treatments.

2.2 Catalyst Synthesis

2.2.1 Inorganic Fraction of LS

The LS samples were dried at 120 °C for 12 h and then calcined at 600 °C for 5 h at a heating rate of 10 °C/min to obtain the inorganic fraction of the sludge. This material was then sieved using a 200-mesh sieve and designated as LS600.

2.2.2 Treatment of LS600 with HCl

LS600 was suspended in a 2 M HCl solution at a solid-to-liquid ratio of 1:10 (solid (g): HCl solution (mL)) and stirred at 300 rpm at room temperature for 30 min. The mixture was then placed in an autoclave at 100 °C for 4 h; after the hydrothermal treatment, the suspension was vacuum-filtered and washed until reaching a pH of ~7. Finally, the solid was dried in an oven at 120 °C for 3 h and calcined at 400 °C for 2 h at a heating rate of 5 °C/min. The material was then sieved using a 200-mesh sieve, and the resulting solid was designated LS600-HCl.

The acid treatment conditions (2 M HCl, 100 °C, 4 h, solid/liquid ratio 1:10) were selected based on a preliminary screening in which LS600 was also treated with 2 M H_2SO_4 under comparable hydrothermal conditions (120 °C, 3 h, same washing and calcination protocol). LS600-HCl yielded higher α-pinene conversion (see Table S1) and a

higher concentration of strong Brønsted acid sites than LS600-H_2SO_4 (see Sect. 3.1). The hydrothermal step at 100 °C for 4 h was adopted to promote deeper dealumination of the tetrahedral Al sites in the anorthite framework and to induce structural reorganization of the silicate phase, generating mesoporosity.

2.2.3 Impregnation of LS600-HCl with Fe

LS600-HCl (1 g) was added to 10 mL of an aqueous suspension containing 0.507 g of $Fe(NO_3)_3 \cdot 9\ H_2O$. After stirring the suspension for 1 h at room temperature, it was dried at 100 °C for 5 h and then calcined at 500 °C for 2 h at a heating rate of 3 °C/min. The resulting solid was designated as LS600-HCl-Fe7%.

The 7 wt% Fe loading was selected based on a preliminary screening of LS600-HCl-based catalysts impregnated with Fe, Ni, and Zn at 3 and 7 wt%, evaluated under identical conditions in the limonene transformation reaction (3 mL limonene, 300 mg catalyst, 165 °C, 24 h, 750 rpm). Among the six screened metal-loaded catalysts, LS600-HCl-Fe7% gave the highest selectivity to *p*-cymene (42%) at complete limonene conversion. The screening results are summarized in Table S2. Blank tests with commercial hematite (Fe_2O_3) and with a silica-supported iron catalyst (Silica-HCl-Fe20%) showed no conversion under these conditions, confirming that the combination of the sludge-derived acid sites, mesoporous structure, and Fe^{3+} species rather than iron oxide alone is responsible for the catalytic activity of LS600-HCl-Fe7%.

2.3 Characterization of Catalysts

The materials were characterized using TGA, XRF, XRD, and SEM-EDS. Textural properties were evaluated using nitrogen adsorption isotherms, and acidity was analyzed by FTIR-Pyridine and TPD-NH_3. Additionally, the Fe phases present in the Fe-impregnated solid were identified by Mössbauer spectroscopy. Thermogravimetric analysis (TGA) of LS was performed on a TGA Q500 V20.13 Build 39 instrument, heating the sample (30.97 mg) from room temperature to 900 °C at a rate of 10 °C/min under a nitrogen flow of 40 mL/min. The chemical composition of LS600, LS600-HCl, and LS600-HCl-Fe7% was determined by X-ray fluorescence (XRF) using a Thermo ARL Optim'X WDXRF spectrometer with Uniquant (semi-quantitative) software. X-ray diffraction (XRD) analyses to identify the crystalline phases present in LS600, LS600-HCl, and LS600-HCl-Fe7% were carried out using a Malvern-PANalytical Empyrean 2012 diffractometer equipped with a Pixel 3D detector and a Cu Kα radiation source (λ = 1.541874 Å) operated at 45 kV and 40 mA; data were collected with a step size of 0.05° and a counting time of 50 s per step.

The morphology of the LS600, LS600-HCl, and LS600-HCl-Fe7% samples was examined by scanning electron microscopy (SEM) using a DENTON VACUUM Desk IV sputter coater and a JSM-6490LV microscope. The samples were coated with a thin gold layer, mounted on graphite tape, and imaged at an accelerating voltage of 11.3 kV. Elemental analysis was carried out using an INCA PentaFETx3 (Oxford Instruments) EDX microprobe. The porous properties of LS600-HCl and LS600-HCl-Fe7% were determined by N_2 adsorption isotherms using a Micromeritics ASAP 2020 PLUS sorptometer. Prior to analysis, the samples were degassed at 350 °C for 4 h under high vacuum. Nitrogen adsorption–desorption isotherms were collected within a relative pressure range of 0.1–0.998 P/P_0. The specific surface area and pore characteristics were calculated using the BET (surface area), Horváth–Kawazoe, and Barrett–Joyner–Halenda method (BJH) (pore volume and pore diameter) methods.

Ammonia Temperature-Programmed Desorption analysis NH_3-TPD was performed using a Micromeritics AutoChem 2920 instrument. The LS600, LS600-HCl, and LS600-HCl-Fe7% samples were treated under a helium flow (50 mL/min), heated to 350 °C at 10 °C/min, and held at this temperature for 30 min. After cooling to 50 °C, the samples were saturated with 0.3% NH_3/He (50 mL/min) for 90 min. The non-chemisorbed ammonia was then removed by purging with helium (50 mL/min) at 50 °C for 45 min. Finally, desorption was carried out by heating the samples to 600 °C at 10 °C/min under a helium flow of 50 mL/min. The Thermal Conductivity Detector (TCD) signal was previously calibrated using ammonia mixtures of known composition.

IR analysis of pyridine adsorption was performed using a Frontier FTIR spectrometer (PerkinElmer, Spectrum 65) equipped with a high-resolution MCT (Mercury Cadmium Telluride) detector and a diffuse reflectance cell (DRIFT). Spectra were collected at a resolution of 4 cm^{-1} in the 1750–1350 cm^{-1} region, averaging 40 scans. The sample was heated to 400 °C (10 °C·min^{-1}) under a helium flow, and background spectra were recorded every 10 °C. After cooling to 40 °C, pyridine adsorption was carried out for 30 min, followed by helium purging for an additional 30 min to remove physisorbed pyridine. The desorption stage was then conducted by heating the sample to 400 °C at 10 °C·min^{-1}, collecting spectra every 10 °C. Finally, the difference between pyridine-adsorbed spectra and the corresponding blanks was calculated, and the Kubelka–Munk transformation was applied to quantify the areas of the relevant bands. This analysis was performed for LS600, LS600-HCl, and LS600-HCl-Fe7%.

For the Mössbauer analysis of LS600-HCl-Fe7%, a spectrometer operating in constant-acceleration mode was used, with a velocity range of ± 11 mm/s and a ^{57}Co source in a rhodium matrix with an initial activity of 25 mCi. Measurements were carried out in transmission geometry at room temperature (25 °C). Obtained data were processed and adjusted with MOSF least squares fitting software.

2.4 Catalytic Evaluation

2.4.1 Isomerization of α-Pinene

In a typical reaction, the catalyst (25–50 mg) with a particle size smaller than 75 µm was added to 1 mL of a 0.25 mmol solution of the terpene in the selected solvent (toluene, cyclohexane, acetonitrile, ethyl acetate, or ethanol) in 2 mL vials. The mixture was magnetically stirred for the selected reaction time (2–5 h) and temperature (70–90 °C. Reaction products were analyzed using an Agilent 7890 A GC–MS system equipped with an FID detector and an Agilent 5975 C mass spectrometer, employing He as the carrier gas and an HP-5MS capillary column (30 m × 0.25 mm × 0.25 µm). The carrier-gas linear velocity and flow rate were 30.5 cm s^{-1} and 2.214 mL min^{-1}, respectively. The oven temperature was maintained at 70 °C for 1 min, then increased to 90 °C at 10 °C·min^{-1} and held for 0.5 min. It was subsequently raised to 110 °C at 10 °C·min^{-1} for 0.5 min, then to 130 °C at the same rate for 0.5 min, and finally to 160 °C at 15 °C·min^{-1} for 1 min. The injection volume was 1 µL in split mode (25:1), with an injector temperature of 250 °C. Compounds were identified using the NIST 5 database. Substrate conversion and selectivity toward the product of interest were calculated using equations Eq. 1 and Eq. 2, respectively.

$$X = \frac{A_{i\ substrato} - A_{t\ Substrato}}{A_{i\ Substrato}} * 100 \quad (1)$$

$$S_j = \frac{A_{t,j}}{A_{i\ Substrato} - A_{t\ Substrato}} * 100 \quad (2)$$

Where X is the conversion of substrate, S_j is the selectivity for the product of interest, A_i is the initial GC area, A_t is the GC area at reaction time t.

2.4.2 Isomerization and Dehydrogenation of Limonene

The isomerization and dehydrogenation of limonene were carried out in a 30 mL round-bottom glass flask equipped with a reflux condenser and a magnetic stirrer. Limonene (3 mL) and the catalyst (200–400 mg, particle size < 75 µm) were added to the reactor and stirred at 750 rpm on a hot plate at 130–165 °C. Reaction products were analyzed using an Agilent 7890 A GC–MS system equipped with an FID detector and an Agilent 5975 C mass spectrometer, employing He as the carrier gas and an HP-5MS capillary column (30 m × 0.25 mm × 0.25 µm). The carrier-gas linear velocity and flow rate were 30.5 cm·s^{-1} and 2.214 mL·min^{-1}, respectively. The oven temperature was maintained at 70 °C for 1 min, then increased to 90 °C at 10 °C·min^{-1} for 0.5 min, followed by increases to 110 °C (10 °C·min^{-1}, 0.5 min), 130 °C (10 °C·min^{-1}, 0.5 min), and 160 °C (15 °C· min^{-1}, 1 min). Finally, the temperature was raised to 190 °C at 15 °C min^{-1} and held for 6.5 min. The injection volume was 1 µL in split mode (25:1), with an injector temperature of 250 °C. Compounds were identified using the NIST 5 database.

Substrate conversion and selectivity to the product of interest were calculated using equations Eq. 3 and Eq. 4, respectively.

$$X = \frac{\sum A_{p-A_s}}{\sum (A_{p+A_S})} * 100 \quad (3)$$

$$S_j = \frac{A_j}{\sum A_p} * 100 \quad (4)$$

Where X is the conversion of substrate, S_j is the selectivity for the product of interest, A_p is the GC area of reaction products and A_S is the GC area of limonene.

2.5 Leaching Tests

To evaluate the heterogeneity of the LS600-HCl and LS600-HCl-Fe7% catalysts in the isomerization of α-pinene and the dehydrogenation of limonene, respectively, the solid catalyst was separated after 10 min of reaction (50 mg of catalyst, 750 rpm, 90 °C) or after 1 h of reaction (200 mg of catalyst, 3 mL of limonene, 750 rpm, 165 °C) using an Advantec syringe filter with a pore size of 0.45 µm. An aliquot of the reaction mixture was analyzed by GC–MS. The reaction was then continued using the filtrate, and additional samples were analyzed by GC–MS after 2, 4, 6, and 8 h for the α-pinene isomerization test, or after 8 and 19 h in the case of the LS600-HCl-Fe7% catalyst.

2.6 Reuse Tests

2.6.1 Isomerization of α-Pinene

Reuse tests were performed on the LS600-HCl catalyst to evaluate its stability. The fresh catalyst was tested under reaction conditions (0.25 mmol α-pinene, 1 mL cyclohexane, 750 rpm, 90 °C, 50 mg catalyst), and after 5 h it was

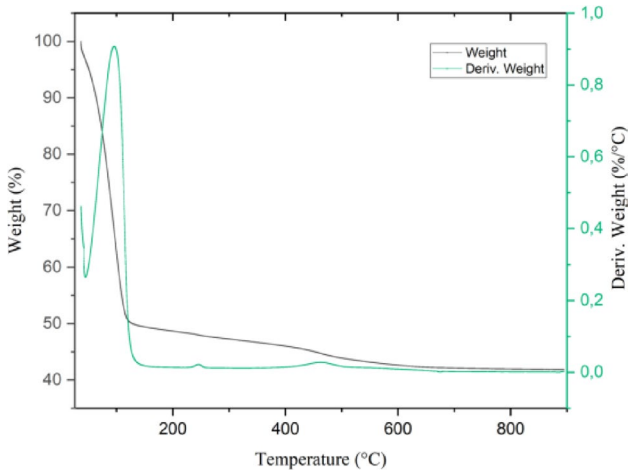

Fig. 1 shows the thermogravimetric analysis of the LS sample, which presents a weight loss of 32.55% attributed to water between 50 °C and 100 °C and between 210 °C and 260 °C. Low-molecular-weight organic molecules (0.78%), followed by the decomposition of higher-molecular-weight organic molecules (3.39%), decompose between 400 °C and 600 °C [1]. The total weight loss of the sample was 57.90%, occurring at temperatures below 600 °C

Table 3 Semi-quantitative Rietveld refinement results for the LS600, LS600-HCl, and LS600-HCl-Fe7% materials

Compound name	Code	% w/w		
		LS600	LS600-HCl	LS600-HCl-Fe7%
Amphibole (Na-Mg)	ICSD 98-016-4666	34	30	30
Anortithe	ICSD 98-000-9330	40	20	19
Albite (heat treated)	ICSD 98-008-7659	11	12	12
Quartz α	ICSD 98-001-6332	7	26	19
Hematite	ICSD 98-001-5840	8	12	12
Magnetite	ICSD 98-008-5806	0	0	6
Maghemite	ICSD 98-004-4517	0	0	2

Semi−quantitative Rietveld refinement

Quality−of−fit parameters: R_expected = 2.43, R_profile = 3.00, R_wp = 3.94, GOF = 2.63

Typical absolute uncertainty for phases present below 5 wt% is ±1–2 wt%

separated and washed twice with 1 mL of cyclohexane and then with ethanol (10 min, 750 rpm, room temperature). Between washes, the solid was recovered by centrifugation (3000 rpm, 10 min). After the final wash, the solid was dried at 80 °C for 12 h and subsequently tested again under the same reaction conditions. The reused solid was designated LS600-HCl-R.

2.6.2 Isomerization and Dehydrogenation of Limonene

To evaluate the stability of the LS600-HCl-Fe7% catalyst, reuse tests were performed. Initially, the fresh catalyst was tested under reaction conditions (3 mL of limonene, 750 rpm, 165 °C, 8 h, 200 mg catalyst). After the reaction, the solid was washed twice with 1 mL of ethanol and stirred for 10 min at 750 rpm and room temperature, then recovered by centrifugation (3000 rpm, 10 min). After the final wash, the solid was dried at 80 °C for 12 h and subsequently used in four additional reaction cycles.

3 Results and Discussion

3.1 Physicochemical Properties of the Catalysts

Figure 1 TGA thermogram of LS material. The figure shows the mass loss curves and the derivative of mass loss of the sample as a function of temperature. An initial decrease in weight is observed, mainly associated with the removal of moisture at low temperatures. Subsequently, additional stages of mass loss occur, related to the decomposition of organic compounds present in the sample, including low- and high-molecular-weight organic molecules. Thermal degradation events are identified by peaks in the DTG curve, indicating different stages of material decomposition as the temperature increases.

The chemical composition of LS600, LS600-HCl, and LS600-HCl-Fe7% determined by XRF analysis is presented in Table S3. Al_2O_3 (33.87% w/w) and SiO_2 (33.32% w/w) are the components present in the highest concentrations in LS600. The elemental percentages of Fe_2O_3, CaO, MgO, Na_2O, TiO_2, K_2O, P_2O_5, and MnO are 7.71% w/w, 1.73% w/w, 1.44% w/w, 1.17% w/w, 1.02% w/w, 0.651% w/w, 0.558% w/w, and 0.161% w/w, respectively. After acid treatment of the LS600 sample, a significant decrease in Al content (down to 8.1% w/w) and an increase in Si concentration in LS600-HCl and LS600-HCl-Fe7% (68.4 and 57.24% w/w, respectively) were observed. As expected, the iron concentration in LS600-HCl-Fe7% (20.31% w/w) was higher than in the untreated LS600 material.

Through Rietveld refinement of the diffractograms, a semi-quantitative analysis of the phases present in the LS600, LS600-HCl, and LS600-HCl-Fe7% samples were obtained. The results of this analysis are presented in Table 3.

The X-ray diffraction patterns of LS600, LS600-HCl, and LS600-HCl-Fe7% are shown in Fig. 2, where every diffraction peak has been labeled with the corresponding phase code (An = amphibole, A = anorthite, Al = albite, H = hematite, C = α-quartz, M = magnetite, Mh = maghemite; full phase names and ICSD codes are given in Table 3). Rietveld

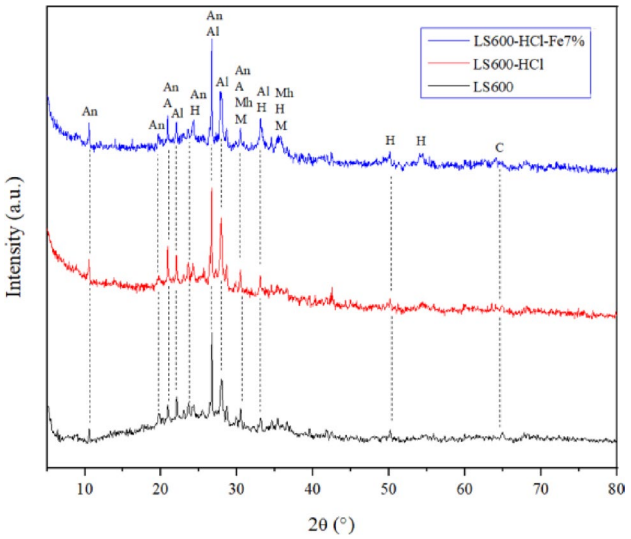

Fig. 2 Minerals identified by XRD in the LS600, LS600-HCl, and LS600-HCl-Fe7% samples. The X-ray diffraction patterns of LS600, LS600-HCl, and LS600-HCl-Fe7% samples show signals associated with anorthite (A) (2θ = 20.92° and 30.48°), α-quartz (C) (2θ = 64.96°), amphibole (An) (2θ = 10.54°, 19.75°, 20.92°, 23.00°, 24.25°, 28.66°, 30.48°, 34.60°, 39.56°, and 50.19°), albite (Al) (2θ = 22.07°, 23.60°, 25.50°, 26.69°, 27.99°, 35.38°, and 41.81°), hematite (H) (2θ = 24.25°, 33.15°, 35.54°, 50.10° and 54.15°), magnetite (M) (2θ = 30.11° and 35.54°) and maghemite (Mh) (2θ = 30.11° and 35.54°). The dotted lines indicate the characteristic positions of the main diffraction peaks identified in the samples

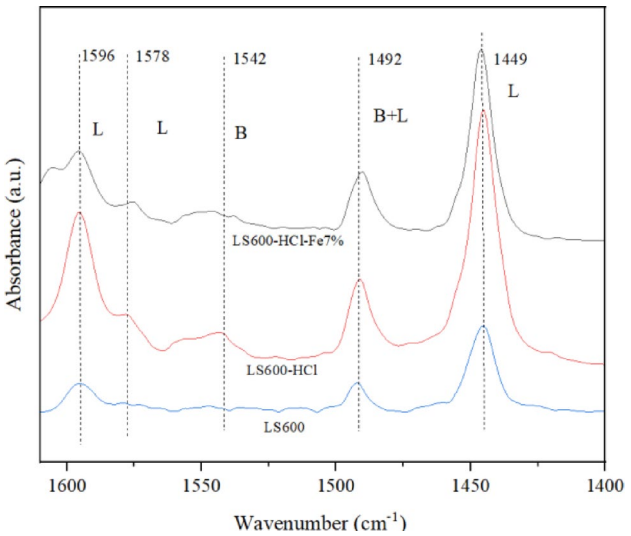

Fig. 3 FTIR-Py spectra of the LS600, LS600-HCl, and LS600-HCl-Fe7% materials at 50 °C. The FTIR spectra of adsorbed pyridine (FTIR-Py) from samples LS600, LS600-HCl, and LS600-HCl-Fe7% show characteristic bands associated with Brønsted and Lewis acid sites. The bands located at 1596, 1578, and 1449 cm^{-1} are attributed to Lewis acid sites (L), while the signal at 1542 cm^{-1} corresponds to Brønsted acid sites (B). The band observed at 1492 cm^{-1} is associated with combined contributions from Brønsted and Lewis acidity (B + L). The dotted lines indicate the positions of the main bands used for the identification of acid sites

refinement of the diffractograms provided a semi-quantitative estimate of the phase composition of the three materials (Table 3). The quality-of-fit parameters (R_expected = 2.43; R_profile = 3.00; R_wp = 3.94; GOF = 2.63) meet the accepted criteria for reliable Rietveld analysis (R_wp < 10, GOF < 4). As this analysis is semi-quantitative, the typical absolute uncertainty for phases present at < 5 wt% is ± 1–2 wt% (Figs. 3, 4 and 5).

The main compositional changes introduced by the acid and Fe treatments are: (i) the anorthite content decreases from 40 wt% in LS600 to ~20 wt% in both LS600-HCl and LS600-HCl-Fe7%, consistent with the removal of tetrahedral Al from the anorthite framework during the HCl-hydrothermal treatment; (ii) this is accompanied by a relative enrichment of the other silicate phases, most notably α-quartz (from 7 wt% to 26 wt% in LS600-HCl); (iii) the impregnation of LS600-HCl with Fe generates two new iron mineralogical phases magnetite (~6 wt%) and maghemite (~2 wt%) in LS600-HCl-Fe7%. The characteristic reflections of magnetite and maghemite (2θ ≈ 30.1° and 35.5°) overlap with the stronger reflections of anorthite (30.48°) and albite (35.38°) in the same region, which limits their direct visual identification in the XRD pattern of LS600-HCl-Fe7%. Their presence is nonetheless unambiguously confirmed by Mössbauer spectroscopy (Fig. 6), which resolves the characteristic sextets of magnetite and maghemite at the concentrations present here.

The acid strength of the materials (LS600, LS600-HCl, and LS600-HCl-Fe7%) was evaluated by NH_3-TPD. Two types of acid strength were observed for LS600 and LS600-HCl-Fe7%, whereas three types were identified for LS600-HCl. Acidity strength is classified according to the NH_3 desorption temperature as weak acidity (100–250 °C), medium acidity (250–400 °C), and strong acidity (400–600 °C) [24]. Fig. S1 shows the experimental signals and the corresponding deconvolutions of the peaks for each material. The appearance of a new signal is associated with the incorporation of additional H^+ ions into the material structure. Moreover, treatment with chlorinated acids results in a slight reduction in the number of weak acid sites and the formation of strong acid sites. Additionally, the incorporation of Fe markedly increases the total acidity of the material, mainly due to the contributions of weak and strong acid sites (Table 4).

The Lewis acid sites associated with the bands at 1596 cm^{-1} and 1449 cm^{-1}, as well as the combined Brønsted–Lewis band at 1492 cm^{-1}, are identified in all solids. Additionally, the band assigned to Lewis acidity at 1578 cm^{-1} appears in all samples except LS600. Finally, a band at 1542 cm^{-1} is observed in LS600-HCl and LS600-HCl-Fe7%, which is attributed to a Brønsted acid site (Fig. 3). These Brønsted sites may form following hydrochloric acid

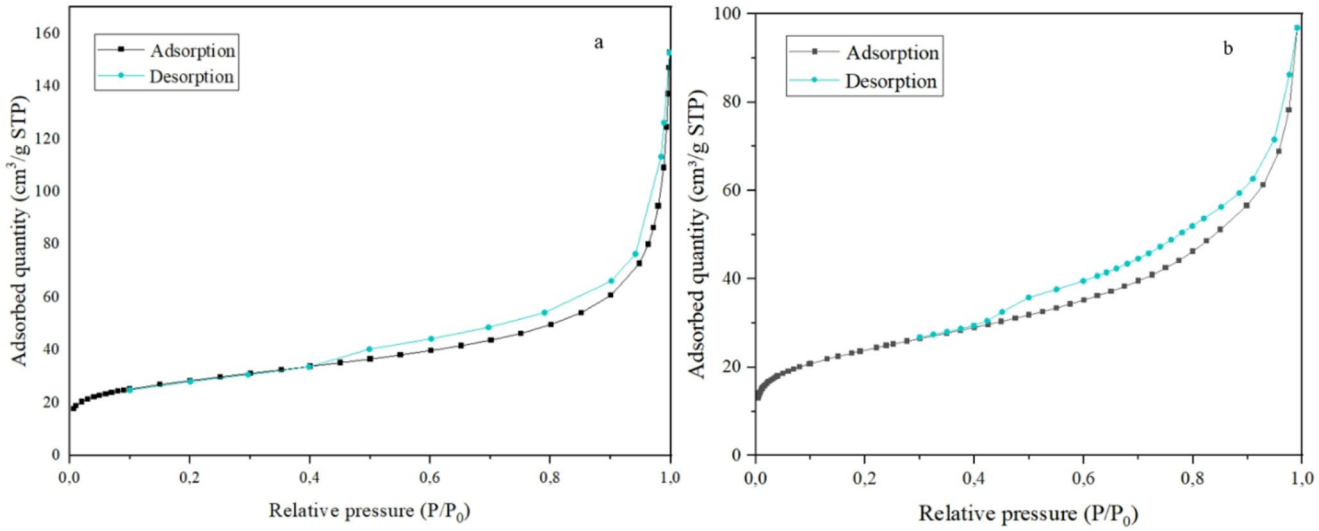

Fig. 4 Adsorption-desorption isotherm of N_2 for the LS600-HCl (**a**) and LS600-HCl-Fe7% (**b**) materials. The nitrogen adsorption–desorption isotherms of samples **a** LS600-HCl and **b** LS600-HCl-Fe7% are presented. The curves show the amount of N_2 adsorbed as a function of relative pressure (P/P_0) along the adsorption and desorption branches. The separation between the two branches gives rise to a hysteresis cycle characteristic of the adsorption–desorption process in porous materials

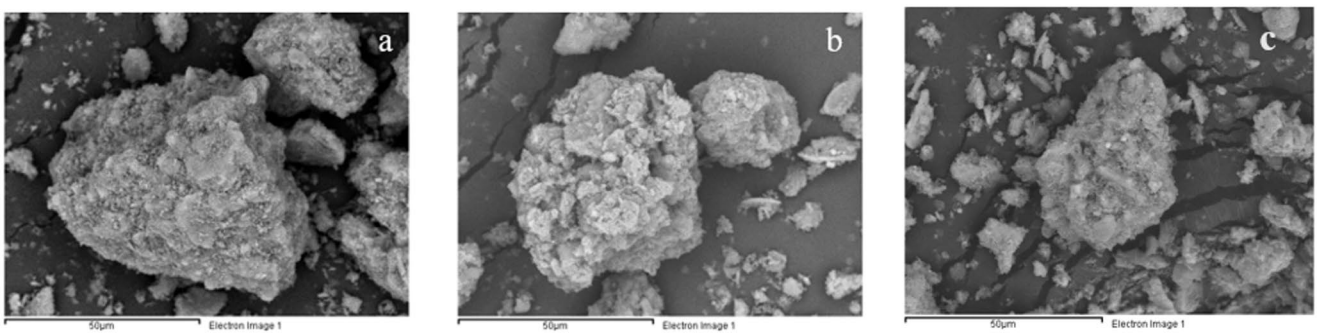

Fig. 5 SEM micrographs of the LS600 (**a**), LS600-HCl (**b**), and LS600-HCl-Fe7% (**c**) samples. Scanning electron microscopy (SEM) micrographs of samples **a** LS600, **b** LS600-HCl, and **c** LS600-HCl-Fe7%. The images show the surface morphology of the materials before and after acid treatment and Fe impregnation. Scale bar: 50 µm

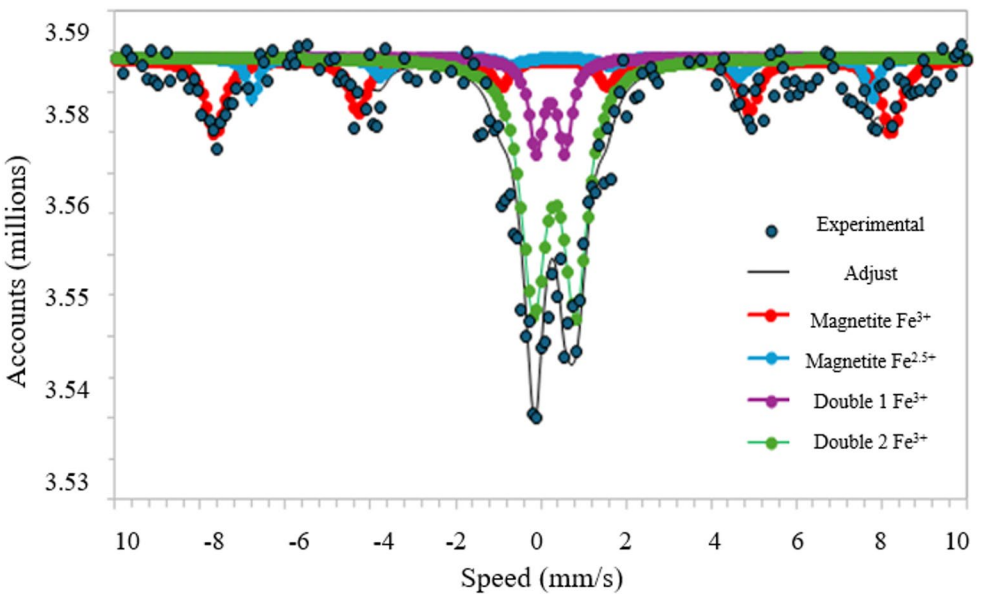

Fig. 6 Mössbauer spectrum at 25 °C for the LS600-HCl-Fe7% sample. Mössbauer spectrum of sample LS600-HCl-Fe7%. The dots correspond to experimental data and the solid line represents the spectrum fit. The fit includes two sextets associated with magnetite phases (Fe^{3+} and $Fe^{2.5+}$) and two doublets corresponding to paramagnetic Fe^{3+} species. The different contributions to the fit are shown with colored lines

Table 4 Distribution of acid strength in the LS600, LS600-HCl, and LS600-HCl-Fe7% materials

Catalyst	Weak acidity (100–250 °C)		Medium acidity (250–400 °C)		Strong acidity (400–600 °C)		Total acidity
	$mmol_{NH3}\ g^{-1}_{catalyst}$	%	$mmol_{NH3}\ g^{-1}_{catalyst}$	%	$mmol_{NH3}\ g^{-1}_{catalyst}$	%	$mmol_{NH3}\ g^{-1}_{catalyst}$
LS600	0.211	73.3	0.00	0	0.075	26.7	285.7
LS600-HCl	0.114	33.8	0.14	40.7	0.086	25.5	337.5
LS600-HCl-Fe7%	0.374	70.8	0.00	0	0.154	29.2	528.2

Table 5 Textural properties and active-site concentrations of the LS600-HCl and LS600-HCl-Fe7% materials

Sample	S_{BET} (m^2/g)	$S_{Mesoporous}$ (m^2/g)	V_p (cm^3/g)[a]	$V_{mesoporous}$ (cm^3/g)	d_p (nm)[b]	Iron content (% w/w)	$\mu mol_{Fe}/m^2$
LS600-HCl	103	71	0.21	0.20	2.6	0	0
LS600-HCl-Fe7%	84	68	0.13	0.13	3.8	20	43

Vp total pore volume, *dp* pore diameter

a Calculated with the BJH method

b Calculated with the Horvath−Kawazoe method

treatment, as the removal of aluminum from the crystalline structure of anorthite generates hydroxyl groups that behave as Brønsted acid sites [25].

The analyzed samples primarily exhibited Lewis acidity, which can be attributed to the presence of aluminum and iron. These metals possess empty or partially filled valence orbitals, enabling them to accept electron pairs from donor molecules or ions. When incorporated into complexes or solid structures, these metals typically exist in positive oxidation states. In these ionic states, Fe and Al exhibit high positive charge densities, which enhances their affinity for electrons donated by neighboring species (such as water molecules or ligands). This interaction polarizes surrounding bonds and facilitates electron acceptance, thereby intensifying the Lewis acid character and increasing the overall acidity of the material [11].

The nitrogen adsorption–desorption isotherms of LS600-HCl and LS600-HCl-Fe7% exhibit Type IV behavior according to IUPAC classification, with an adsorption branch at $P/P_0 > 0.5$ and a hysteresis loop characteristic of multilayer adsorption and capillary condensation in mesopores (Fig. 4). Table 5 summarizes the textural properties and iron content of the two materials. Both samples exhibit a predominance of mesopores, as confirmed by their pore-size distributions (Fig. S2a and Fig. S2b). After Fe impregnation, the BET surface area decreases from 103 m²/g (LS600-HCl) to 84 m²/g (LS600-HCl-Fe7%) and the total pore volume decreases from 0.21 to 0.13 cm³/g, consistent with partial pore occupation by iron species. The iron loading of LS600-HCl-Fe7% is 20 wt% (from XRF), which on a surface-area basis corresponds to 43 µmol_Fe/m². We note that this surface loading does not directly establish a well-dispersed distribution of iron, and that iron dispersion was not quantified in this study. EDS mapping (Fig. S3) indicates that Fe is distributed across the analyzed regions together with Si and Al. The catalytic performance reported hereafter should therefore be interpreted as reflecting the combined effect of iron content, acid-site distribution, and mesoporous texture, rather than a well-defined Fe dispersion.

The micrographs reveal non-homogeneous surfaces; LS600 exhibits a coarse morphology, whereas LS600-HCl displays increased surface porosity and more prominent protuberances (Fig. 5). Despite the more irregular and undefined texture observed in LS600-HCl-7%, no substantial morphological transformations were identified as a result of the acid treatment or Fe loading.

The Mössbauer spectrum of LS600-HCl-Fe7% was recorded in transmission geometry at room temperature and processed with the MOSF least-squares fitting software to identify the iron-containing phases and to quantify their relative abundance in the material (Fig. 6). The spectrum was fitted using two sextets and two doublets. The two sextets exhibit hyperfine parameters characteristic of magnetite: one corresponding to tetrahedral sites occupied by Fe^{3+} ions, and the other to octahedral sites occupied by $Fe^{2.5+}$ intermediate valence ions. At room temperature, this intermediate valence arises from electron hopping between neighboring octahedral sites occupied by Fe^{3+} and Fe^{2+} ions. Because the Mössbauer transition occurs on a timescale (10^{-8} to 10^{-9} s) faster than the relaxation time of this hopping, an average oxidation state is observed. This oxidation state is further corroborated by the isomer shifts (δ) of both sextets. The Fe^{3+} sextet may also include a contribution from maghemite (γ-Fe_2O_3), a highly oxidized form of magnetite commonly found in samples exposed to oxygen-rich atmospheres. According to the fitting results, the magnetite-maghemite phases account for 36% of the sample, with 28% attributed to Fe^{3+} (magnetite/maghemite) and 8% to $Fe^{2.5+}$ (magnetite). Doublets 1 and 2 correspond to paramagnetic phases containing Fe^{3+}. These cannot be uniquely identified by

room-temperature Mössbauer spectroscopy alone, as their hyperfine parameters are consistent with both superparamagnetic goethite (α-FeOOH) and hematite (α-Fe_2O_3) [26]. However, based on the X-ray diffraction results (Fig. 2), these paramagnetic phases are identified as hematite. Collectively, these phases represent 64% of the sample (12% for Doublet 1 and 52% for Doublet 2).

3.2 Catalytic Production of Camphene from α-Pinene

The influence of various reaction conditions on the synthesis of camphene from α-pinene was evaluated, and catalyst stability was investigated through leaching and reuse tests. Additionally, a statistical analysis of substrate conversion and selectivity toward camphene is presented, alongside a proposed reaction scheme.

3.2.1 Effect of the Solvent

Table 6 summarizes the influence of the solvent on the catalytic isomerization of α-pinene over LS600-HCl. No reaction occurred in the presence of polar solvents such as acetonitrile, ethyl acetate, or ethanol. Among the nonpolar media evaluated, cyclohexane provided the highest α-pinene conversion and the greatest selectivity toward camphene. The superior performance of cyclohexane compared to toluene may be related to differences in how these solvents stabilize the carbocationic intermediate formed upon coordination of the monoterpene's C = C bond with the acid sites. The aromatic structure of toluene could modify the stabilization environment or compete more strongly for adsorption sites, affecting the strength and nature of the adsorption relative to cyclohexane. Such variations in adsorption behavior may ultimately influence the observed selectivity toward camphene [11].

3.2.2 Effect of Temperature

At 80 °C, the conversion reached 12%, while at 90 °C it increased to 30%. The selectivity toward camphene remained essentially constant at approximately 38% across the evaluated temperature range. This behavior is consistent with the expected increase of the reaction rate constant with temperature (Fig. 7a). Previous studies support this trend; for example, it was reported [10] that varying the temperature from 20 °C to 200 °C (7 h, 10% Ti-SBA-15 relative to α-pinene) led to an increase in α-pinene conversion up to a maximum of 60% at 180 °C, followed by a slight decrease to 55% at 200 °C, attributed to temperatures approaching the boiling point of the reaction mixture. Similarly, using a CLIN 0.1 catalyst (1 h, 7.5 wt% catalyst), α-pinene conversion increased from 89% to 99% when the temperature was increased from 70 °C to 80 °C. In this case, selectivity toward camphene (53–55%) and limonene (29–31%) remained nearly unchanged within the 30–80 °C range [8]. Overall, the results demonstrate that temperature significantly influences α-pinene conversion, but exerts only a minor effect on product selectivity under the conditions investigated.

3.2.3 Effect of Reaction Time

As the reaction progressed, the selectivity toward limonene increased to 35%, together with the formation of minor isomerization products such as terpinolene (11%) (Fig. 7b). These products are consistent with the predominance of Lewis acid sites in the studied catalyst, which favor skeletal rearrangements of monoterpenes. Miądlicki et al. [8] reported a markedly faster reaction using the CLIN 0.1 catalyst, where α-pinene was fully converted within 210 s under their conditions. In their study, product selectivity varied significantly during the first 30–270 s of reaction, but remained unchanged at longer times.

3.2.4 Effect of Catalyst Amount

Increasing the amount of catalyst enhances the availability of Brønsted and Lewis acid sites, which in turn promotes α-pinene conversion. (Fig. 7c). Previous studies reported similar behavior; for example, it is reported [10] that α-pinene conversion reached a maximum of 95% at a Ti-SBA-15 loading of 15 wt%; further increasing the catalyst content to 20 wt% did not improve conversion but promoted the formation of polymeric by-products. Likewise, when the concentration of the CLIN 0.1 catalyst was varied

Table 6 Effect of the solvent on the catalytic isomerization of α-pinene over the LS600-HCl catalyst

Solvent	Polarity	% X	% Selectivity							
			Camphene	β-Pinene	α-Felandrene	*p*-Cymene	Limonene	3-Carene	Terpinolene	Others
Acetonitrile	Polar	0	0	0	0	0	0	0	0	0
Ethyl acetate	Polar	0	0	0	0	0	0	0	0	0
Ethanol	Polar	0	0	0	0	0	0	0	0	0
Toluene	Non polar	10	27	0	3	2	68	0	0	0
Cyclohexane	Non polar	30	38	1	2	2	35	1	2	18

Reaction conditions: 0.25 mmol α−pinene (98%), 1 mL solvent, 750 rpm, 90 °C, 2 h, 25 mg LS600−HCl

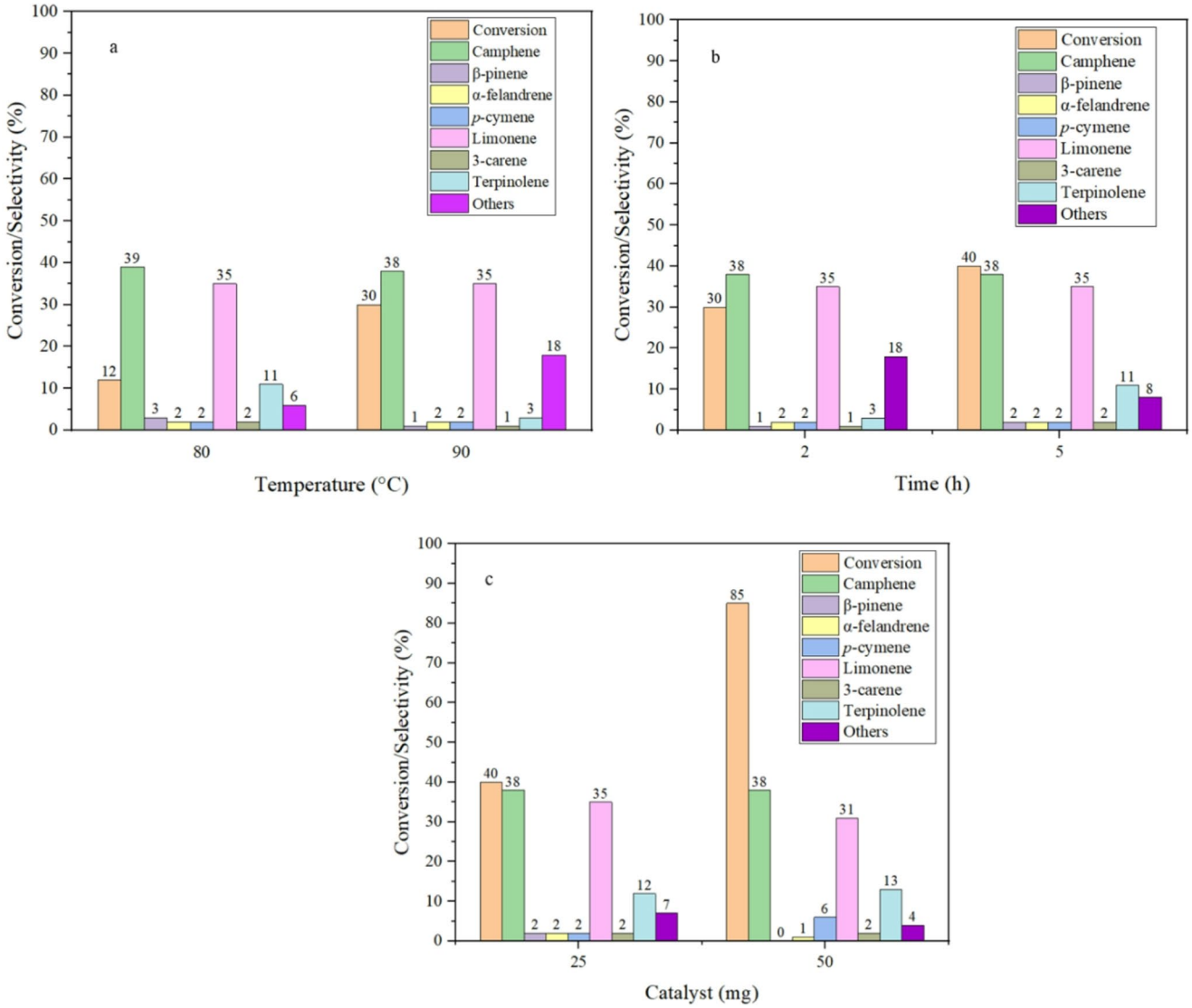

Fig. 7 Main effects on the conversion of α-pinene and the selectivity of isomerization products. Conversion of α-pinene and selectivity toward the main reaction products on the LS600-HCl catalyst as a function of **a** temperature, **b** reaction time, and **c** catalyst amount. The bars correspond to the conversion of α-pinene and selectivity towards camphene, β-pinene, α-phellandrene, *p*-cymene, limonene, 3-carene, terpinolene, and other products. Reaction conditions: 0.25 mmol α-pinene, 1 mL cyclohexane, 90 °C (**b** and **c**), 25 mg catalyst (**a** and **b**), 5 h (**a** and **c**), and 750 rpm

between 2.5 and 12.5 wt% at 70 °C, complete conversion was achieved with 10 wt% catalyst [8]. In that study, camphene selectivity remained unchanged for catalyst loadings above 7.5 wt%, although increased isomerization of limonene to α- and γ-terpinene, terpinolene, and *p*-cymene was observed.

Studies on the effects of temperature and catalyst loading indicate an interplay between these variables: higher temperatures reduce the amount of catalyst required to achieve high α-pinene conversions, whereas increasing the catalyst loading allows comparable conversions to be reached at lower temperatures. Under all evaluated conditions, camphene selectivity remained essentially constant at approximately 38%, likely due to the combined action of Brønsted and Lewis acid sites, which are both necessary for the rearrangement of α-pinene [11]. Because LS600-HCl contains a relatively low concentration of Brønsted acid sites, these are rapidly saturated by the camphene-forming pathway, while the remaining Lewis acid sites promote competing isomerization reactions. Similar behavior has been reported for Ti-SBA-15, where camphene selectivity remained nearly constant at around 27% despite variations in reaction parameters [10].

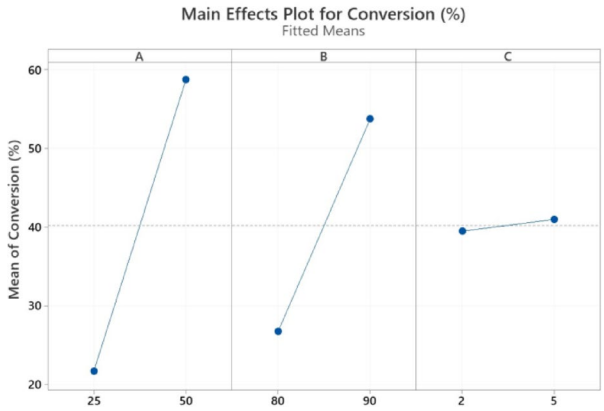

Fig. 8 Graph of main effects for the conversion-isomerization of α-pinene. Prepared using Minitab® software. Graph of main effects for the conversion of α-pinene. The graph shows the effect of reaction variables on average conversion: **A** amount of catalyst in mg, **B** temperature in °C, and **C** reaction time in h

3.2.5 Statistical Analysis of the Effect of Reaction Conditions

The main-effects plot (Fig. 8) provides an exploratory, screening-level assessment of the relative influence of the operational variables on α-pinene conversion over LS600-HCl within the tested range. Within this range, increasing the catalyst amount leads to the most pronounced rise in conversion, consistent with the greater availability of acid sites; the effect of temperature is moderate; and the effect of reaction time is relatively weak. Camphene selectivity remained essentially constant at ~38% across all tested conditions. We emphasize that a two-level factorial design captures trends but does not permit the identification of optima or non-linear responses. A detailed response-surface study over a wider range of catalyst loadings and temperatures is recommended for process optimization, and would also help to identify the onset of mass-transport limitations expected at higher catalyst-to-substrate ratios.

3.2.6 Leaching and Reuse Tests

The conversion remained essentially unchanged at 3.7% after the catalyst was removed from the reaction mixture at 10 min, indicating that no active species were leached into the liquid phase. In contrast, when the catalyst remained in the system, the conversion reached 85% after 5 h of reaction (Fig. 9a). These results confirm that the catalytic activity arises exclusively from the solid phase and that LS600-HCl operates as a truly heterogeneous catalyst.

As shown in Fig. 9b, α-pinene conversion decreased progressively with reuse cycles, from 83% over the fresh catalyst to 28% after the fourth cycle, whereas camphene selectivity remained essentially constant at around 38% throughout the stability test. This pattern loss of activity without a change in the product distribution suggests that deactivation does not involve a chemical modification of the acid sites of the catalyst, but rather a reduction in the number of sites accessible to the substrate.

The FTIR-Py spectra of fresh LS600-HCl and reused LS600-HCl-R (recovered after the fourth cycle), recorded at 50 °C, are shown in Fig. 10. Both spectra display the characteristic bands of pyridine coordinated to Lewis sites (1449 and 1596 cm^{-1}), pyridine protonated on Brønsted sites (1542 cm^{-1}), and the combined band associated with both site types (1492 cm^{-1}). A rigorous quantitative comparison of these spectra is not appropriate in this case, since the absolute band intensities depend on experimental variables

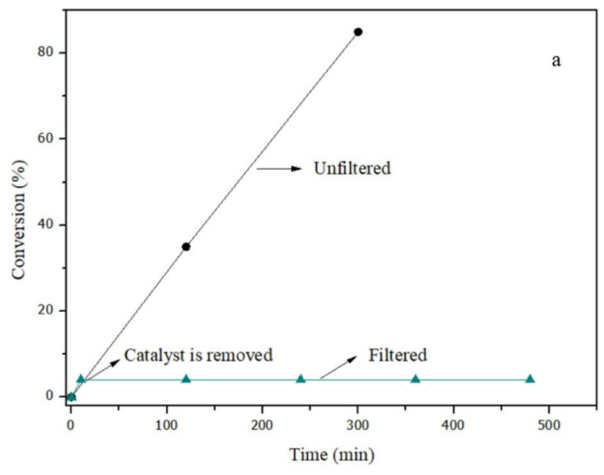

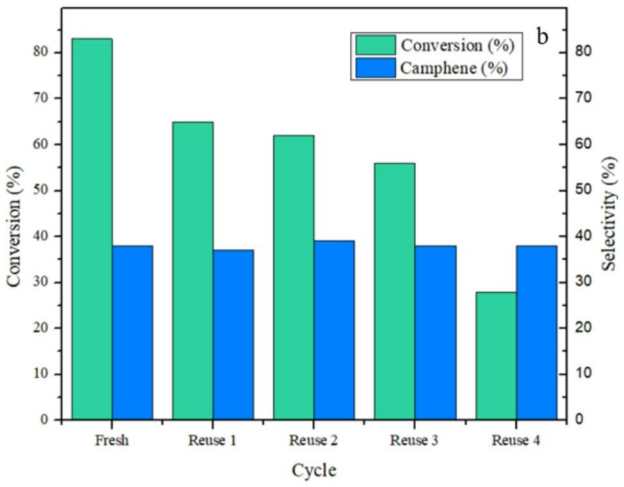

Fig. 9 Leaching test for LS600-HCl (**a**). Reuse test for LS600-HCl (**b**). **a** Leaching test to evaluate the heterogeneous nature of the LS600-HCl catalyst. The catalyst was removed from the reaction mixture after 10 min and the reaction was allowed to continue under the same conditions. **b** Reuse of the LS600-HCl catalyst in the conversion of α-pinene for four consecutive cycles. Reaction conditions: 0.25 mmol α-pinene, 1 mL cyclohexane, 90 °C, 750 rpm, and 50 mg catalyst

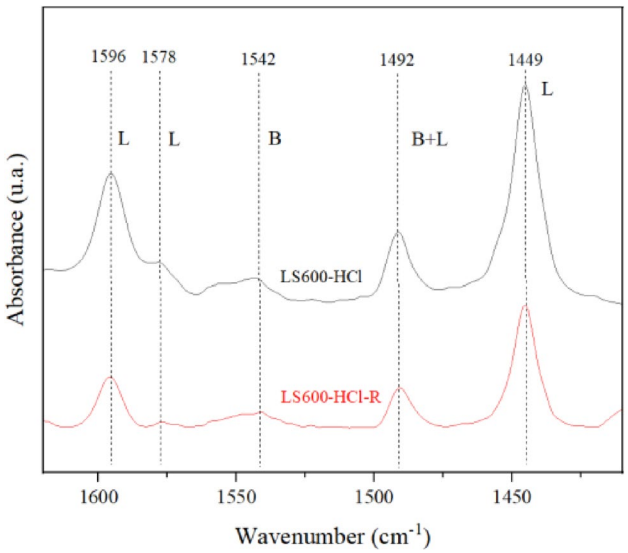

Fig. 10 FTIR-Py spectra LS600-HCl-R and LS600-HCl at 50 °C. FTIR spectra of adsorbed pyridine (FTIR-Py) from fresh and reused LS600-HCl samples recorded at 50 °C. The bands located at 1596, 1578, and 1449 cm^{-1} are attributed to Lewis acid (L) sites, while the band at 1542 cm^{-1} corresponds to Brønsted acid (B) sites. The signal observed at 1492 cm^{-1} is associated with combined contributions from Brønsted and Lewis acidity (B + L)

that were not strictly controlled during acquisition, in particular the ambient humidity and the amount of solid loaded into the DRIFT cell, which was not identical for both samples. The comparison between the two samples is therefore restricted to a qualitative interpretation.

From this qualitative perspective, the relevant observation is that the full set of bands associated with adsorbed pyridine Brønsted at 1542 cm^{-1}, Lewis at 1449 and 1596 cm^{-1}, and the combined band at 1492 cm^{-1} remains present in the spectrum of the reused catalyst. This indicates that the chemical nature of the acid sites is preserved after the reaction cycles, and that the decrease in conversion cannot be attributed to a structural loss or to an irreversible chemical transformation of the Brønsted or Lewis sites of the catalyst.

A more consistent explanation, in agreement with the full set of experimental observations, is the gradual blocking of the active sites by heavy organic species formed during the reaction and retained on the surface and within the mesopores of the catalyst. This interpretation is supported by several converging observations. First, the material exhibits a moderate surface area (103 m^2/g) dominated by mesopores with an average diameter of 2.6 nm (Table 5), a size range that is particularly susceptible to blocking by oligomeric and polymeric species derived from terpenes. Second, α-pinene isomerization proceeds through pinyl and bornyl carbocation intermediates, which are well-known precursors of parallel oligomerization reactions in the presence of acid sites [8, 17]. Third, the chromatograms of the reaction mixture systematically show heavy products grouped as "others" in the selectivity distributions (Table 6), consistent with the formation of oligomeric species that may remain adsorbed in the catalyst pores between reaction cycles. Finally, this physical-blocking interpretation is fully consistent with the preservation of camphene selectivity across the stability test, since an approximately uniform deposition of organic species on the surface reduces the number of accessible sites without altering the relative proportion of Brønsted and Lewis sites or modifying the reaction pathways that govern the product distribution.

3.2.7 Proposed Reaction Scheme

A reaction scheme is proposed in Fig. 11 based on catalyst characterization, catalytic performance, literature reports [6, 8, 10], and the reaction products identified in this study (Fig. 7c, Fig. S4). α-Pinene is a bicyclic monoterpene whose endocyclic double bond and strained bicyclo[3.1.1] heptane framework make it highly susceptible to acid-catalyzed isomerization (Fig. 11). The scheme begins with the interaction of α-pinene with the Brønsted acid sites of the LS600-HCl catalyst, promoting the opening of the cyclopropane ring and generating a highly unstable pinyl-type carbocation. This intermediate can rearrange to form a pinylcarbonium ion [8], which subsequently reorganizes to produce a bornylcarbonium ion; the latter undergoes deprotonation to yield camphene [6].

From the same carbocationic intermediate, alternative rearrangement pathways lead to the formation of other observed products. The formation of 3-carene proceeds through a skeletal rearrangement in which the cyclic framework is reorganized and reclosed to produce the characteristic bicyclic structure of this monoterpene. Similarly, deprotonation of the carbocation followed by double-bond rearrangement leads to limonene, characterized by a six-membered ring bearing one endocyclic and one exocyclic double bond. Further isomerization of limonene affords α-phellandrene and terpinolene, while consecutive dehydrogenation (loss of 2 H^+) results in the formation of *p*-cymene [8, 10].

3.3 Catalytic Production of *p*-Cymene from Limonene

The influence of different reaction conditions on the synthesis of *p*-cymene from limonene was systematically evaluated, and the stability of the catalyst was assessed through leaching and reuse tests. In addition, a statistical analysis of substrate conversion and *p*-cymene selectivity was performed to identify the most influential operational variables.

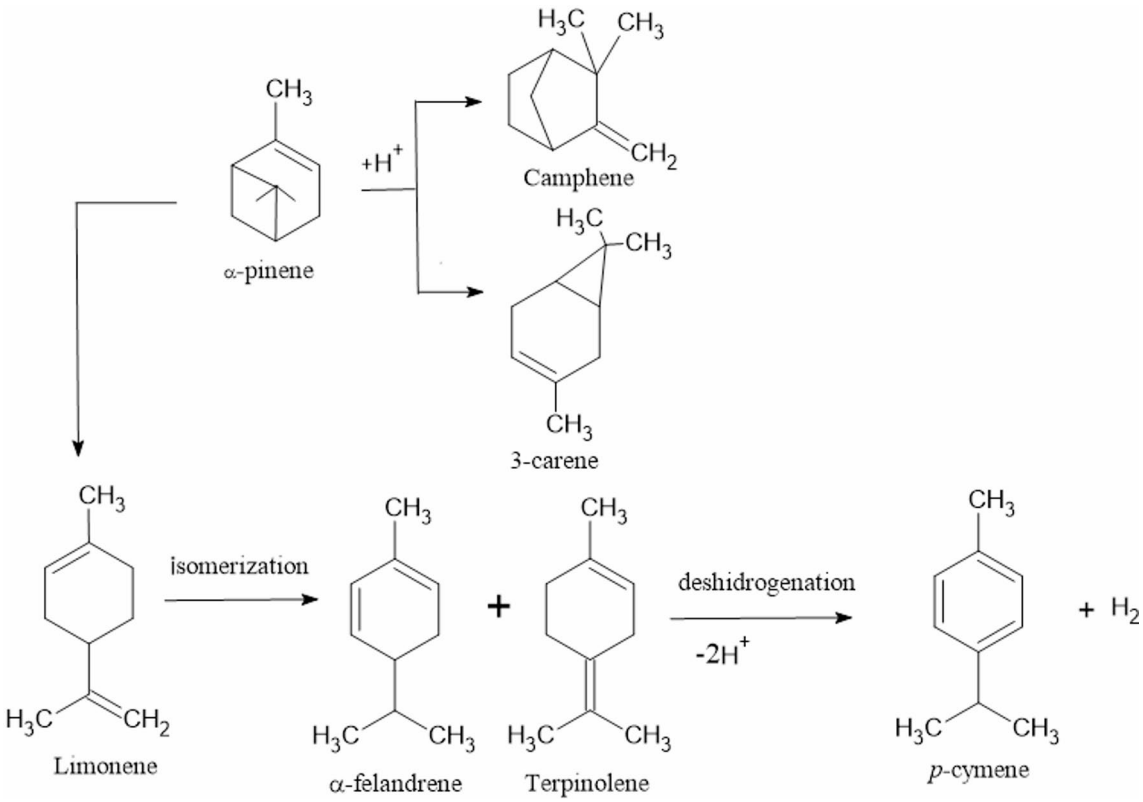

Fig. 11 General scheme of the isomerization reaction of α-pinene with the LS600-HCl catalyst. Based on [8]. Proposed scheme for the acid isomerization of α-pinene on the LS600-HCl catalyst, showing the main reaction pathways to camphene, 3-carene, limonene, α-phellandrene, terpinolene, and *p*-cymene

Finally, a reaction-route scheme is proposed based on experimental observations, catalyst characterization, and literature reports.

3.3.1 Effect of the Reaction Temperature

The conversion of limonene remained constant at 100% at both tested temperatures (130 and 165 °C). However, *p*-cymene selectivity increased from 32% at 130 °C to 44% at 165 °C (Fig. 12a). This trend suggests that higher temperatures favor the disproportionation of *p*-ment-3-ene (4%) and enhance the dehydrogenation pathway leading to *p*-cymene, an endothermic process. Similar temperature dependent behavior has been reported in the literature. For example, Retajczyk [21] showed that after 24 h of reaction over a Ti-MCM-41 catalyst, limonene conversion increased from 92% to 96% and *p*-cymene selectivity rose from 7% to 46% when the temperature was increased from 160 °C to 170 °C. In another study [23], *p*-cymene selectivity reached 92% at 200 °C and 100% at 250 °C using a 20% CdO/SiO_2 catalyst.

3.3.2 Effect of Reaction Time

Figure 12b shows that increasing the reaction time from 8 to 24 h leads to an increase in conversion from 70% to 100%, while *p*-cymene selectivity rises from 20% to 30%. Longer reaction times also result in higher selectivities toward secondary products, namely 15% for *p*-ment-3-ene, 5% for *cis*-ment-8-ene, and 31% for polymeric species. This behavior can be attributed to the occurrence of consecutive reactions involving both limonene and its primary isomerization products. The observed increase in limonene conversion and in *p*-cymene selectivity is consistent with reports in the literature; for instance, using a Ti-MCM-41 catalyst, conversion values up to 96% and *p*-cymene selectivity of 46% were obtained after extending the reaction time to 24 h [21].

3.3.3 Effect of the Amount of Catalyst

Figure 12c shows that limonene conversion remains constant at 100% for both tested catalyst loadings (200 and 400 mg). In contrast, *p*-cymene selectivity decreases from 44% to 30% when the catalyst amount is increased from 200 mg to 400 mg. This decline in selectivity is likely associated with the enhanced contribution of side reactions at

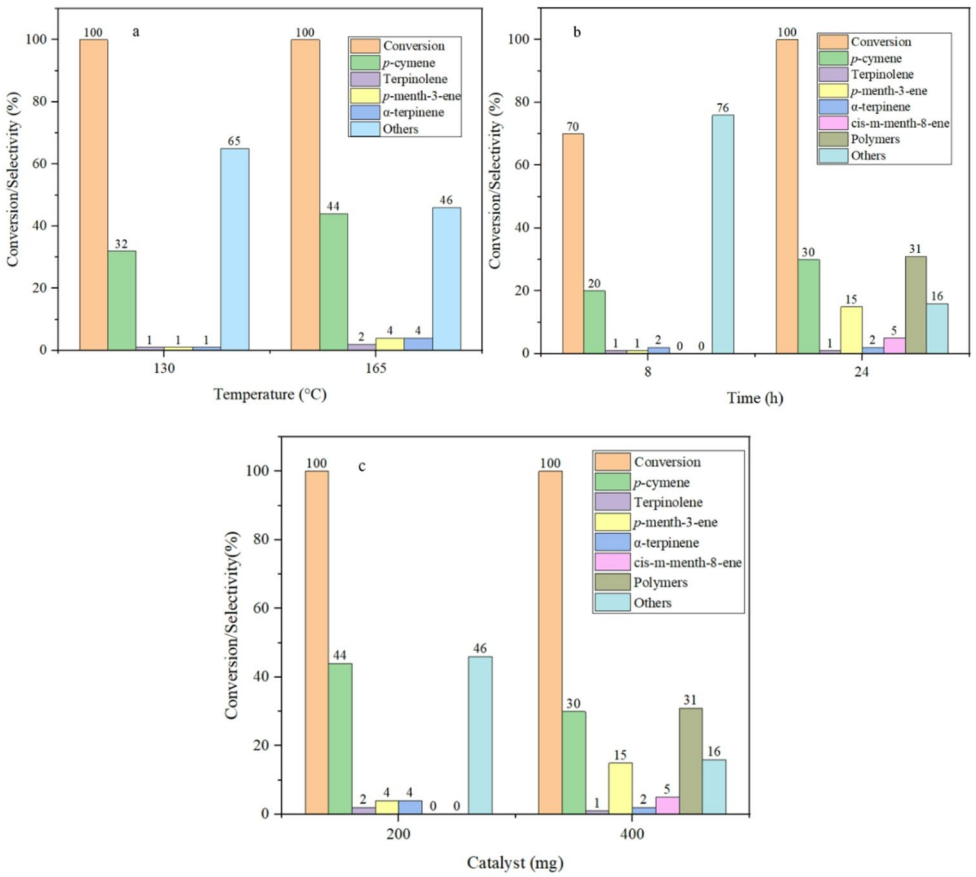

Fig. 12 Main effects on limonene conversion and selectivity of isomerization and dehydrogenation products. Limonene conversion and selectivity toward the main reaction products on the LS600-HCl-Fe7% catalyst as a function of **a** reaction temperature, **b** reaction time, and **c** catalyst amount. The bars represent limonene conversion and selectivity towards *p*-cymene, terpinolene, *p*-menth-3-ene, α-terpinene, cis-menth-8-ene, polymeric species, and other products. Reaction conditions: 3 mL limonene, 200 mg catalyst (**a** and **b**), 165 °C (**b** and **c**), 750 rpm, and 24 h (**a** and **c**)

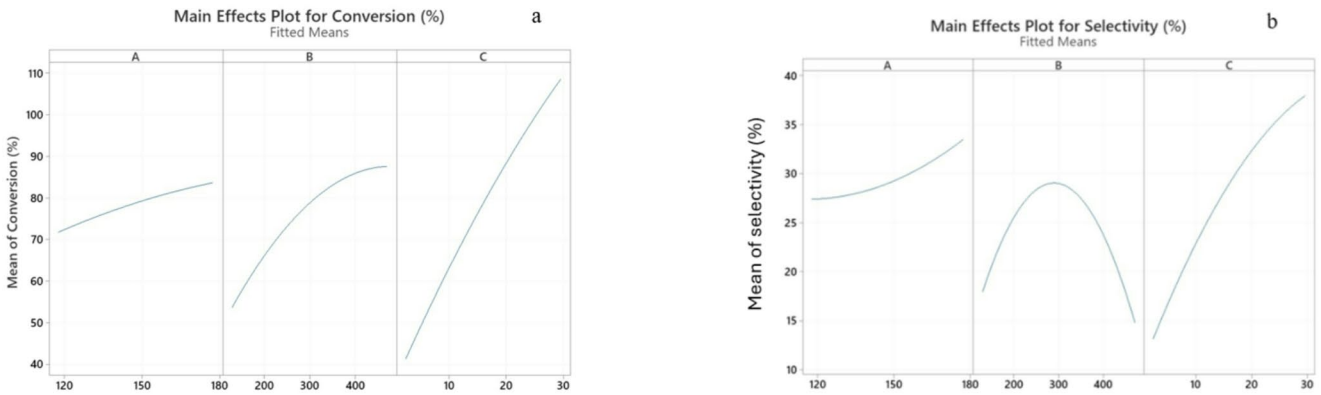

Fig. 13 Graphs of main effects. Elaboration using Minitab® software. Main effect graphs for reaction conditions. **a** Effect of reaction variables on limonene conversion. **b** Effect of reaction variables on selectivity towards *p*-cymene. The factors evaluated correspond to: (A) temperature (°C), (B) amount of catalyst (mg), and (C) reaction time (h)

higher catalyst loadings. Based on these results, the reaction conditions that maximize both limonene conversion and *p*-cymene selectivity are 24 h of reaction time, 165 °C, and 200 mg of catalyst.

The observation that increasing the catalyst loading from 200 to 400 mg does not improve p-cymene selectivity but increases the contribution of side reactions (polymers, 31%; *p*-menth-3-ene, 15%) is consistent with the expected onset of diffusional limitations and enhanced secondary chemistry at high catalyst-to-substrate ratios in a liquid-phase batch system. This behavior also supports the choice of 200 mg as the reference loading for the subsequent studies.

3.3.4 Statistical Analysis of the Effect of Reaction Conditions

Figure 13a shows the main-effects plot for limonene conversion, from which it can be concluded that temperature,

catalyst loading, and reaction time all exert a positive influence on conversion. Among these variables, reaction time has the strongest effect, whereas temperature exhibits only a minor impact within the evaluated range. Conversion increases with catalyst loading up to 400 mg, beyond which no further changes were detected.

From Fig. 13b, it can be concluded that all three factors have a significant impact on *p*-cymene selectivity. Both temperature and reaction time exert a positive effect, with reaction time being the most influential variable. In contrast, catalyst loading displays a maximum in its effect on selectivity, likely due to the promotion of competing reaction pathways at higher catalyst amounts.

3.3.5 Leaching and Reuse Tests

The conversion remained essentially unchanged at 10% after the catalyst was removed from the reaction mixture at 1 h, indicating that no active species were leached into the liquid phase (Fig. 14a). In contrast, when the catalyst was left in the system, the conversion reached 100% after 24 h of reaction. These findings demonstrate that the catalytic activity originates exclusively from the solid phase and confirm that LS600-HCl-Fe7% operates as a truly heterogeneous catalyst.

Reuse tests of the LS600-HCl-Fe7% catalyst show that *p*-cymene selectivity remains nearly constant at approximately 24% across all cycles (Fig. 14b), indicating that the catalyst maintains good chemical stability with respect to product distribution. In contrast, limonene conversion remains stable at ~68% up to the second reuse, after which an 18% decrease is observed, dropping from 68% to 56% over the last two reaction cycles. Overall, these results demonstrate that the catalyst exhibits satisfactory stability in terms of both limonene conversion and selectivity toward *p*-cymene, despite some loss of conversion upon successive reuse.

3.3.6 Scheme and Proposed Reaction Route

Based on catalyst characterization, catalytic tests, literature reports [20, 27], and the reaction products identified in this work (Fig. 12c, Fig. S7), a general reaction scheme for the isomerization and dehydrogenation of limonene is proposed (Fig. 15). In most cases, *p*-cymene formation from limonene begins with the isomerization of limonene into other terpene intermediates, which occurs through migration of the exocyclic double bond into the ring (pathway I). These intermediates subsequently undergo dehydrogenation of the carbocyclic ring to yield *p*-cymene. Additionally, disproportionation of limonene (pathway II) and of terpene intermediates such as terpinolene, α-terpinene, *p*-ment-3-ene, and *cis*-ment-8-ene also contributes to *p*-cymene formation through subsequent dehydrogenation. Large quantities of high-molecular-weight "polymeric" products are also formed (pathway III), arising from polymerization reactions of limonene and its intermediates. Isomerization, disproportionation, and polymerization occur on the acidic sites of the catalyst via carbenium-ion mechanisms. In contrast, the dehydrogenation step taking place on metal sites is endothermic, requiring relatively high temperatures to achieve acceptable yields of *p*-cymene. Because these pathways are all promoted by acidic sites, competitive and simultaneous reactions proceed across the three routes [27, 28].

For the formation of *p*-cymene, a bifunctional catalyst containing both acid and metal sites is required. The

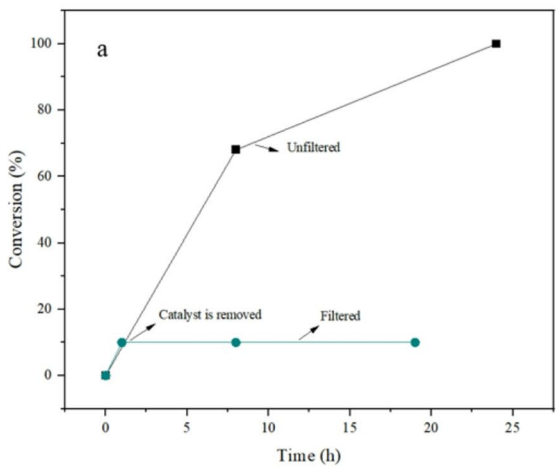

Fig. 14 Leaching test for LS600-HCl-Fe7% (**a**). LS600-HCl-Fe7% reuse test (**b**). **a** Leaching test performed to evaluate the heterogeneous nature of the LS600-HCl-Fe7% catalyst. The catalyst was removed from the reaction mixture after 1 h and the reaction was allowed to continue under the same conditions. **b** Reuse of the LS600-HCl-Fe7% catalyst in the conversion of limonene and selectivity towards *p*-cymene during consecutive reaction cycles. Reaction conditions: **a** 3 mL of limonene, 200 mg of catalyst, 165 °C, and 750 rpm; **b** 3 mL of limonene, 300 mg of catalyst, 165 °C, 750 rpm, and 8 h

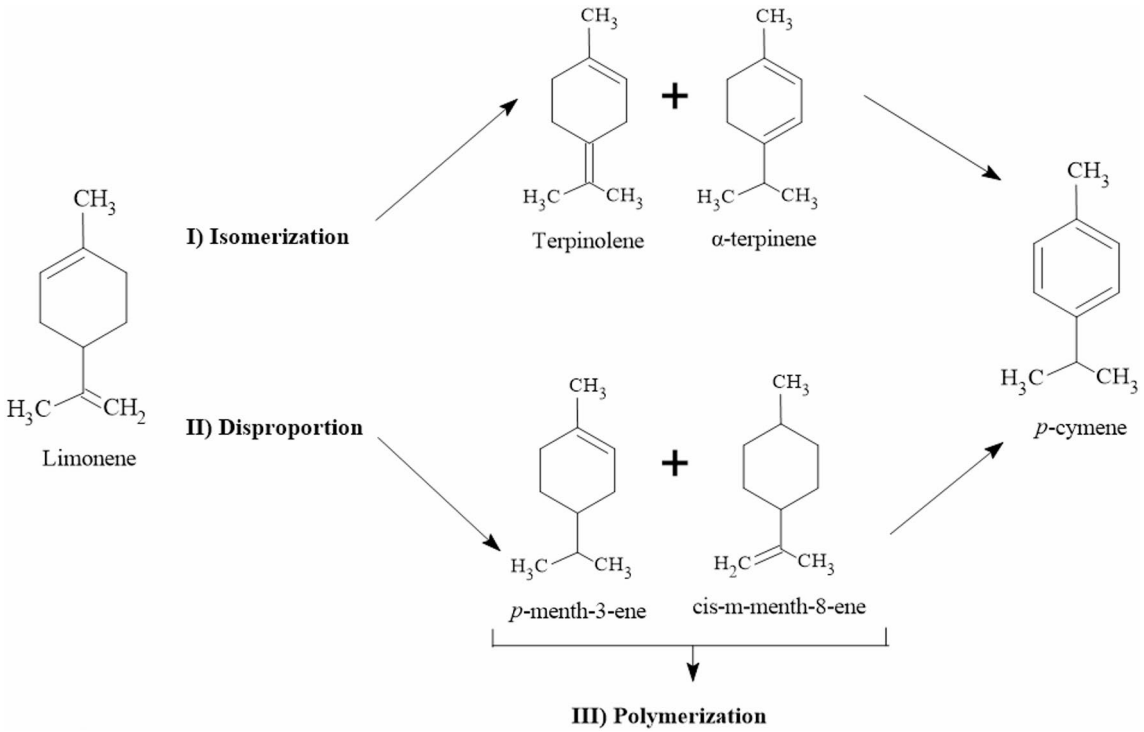

Fig. 15 General reaction scheme for the isomerization and dehydrogenation of limonene, based on [20, 27]. General reaction scheme proposed for the isomerization and dehydrogenation of limonene to *p*-cymene. The formation of *p*-cymene can proceed via: (I) isomerization of limonene to terpenic intermediates followed by dehydrogenation; (II) disproportionation reactions that generate intermediates such as *p*-ment-3-ene and cis-ment-8-ene, which are subsequently dehydrogenated to *p*-cymene; and (III) polymerization reactions that lead to high molecular weight products

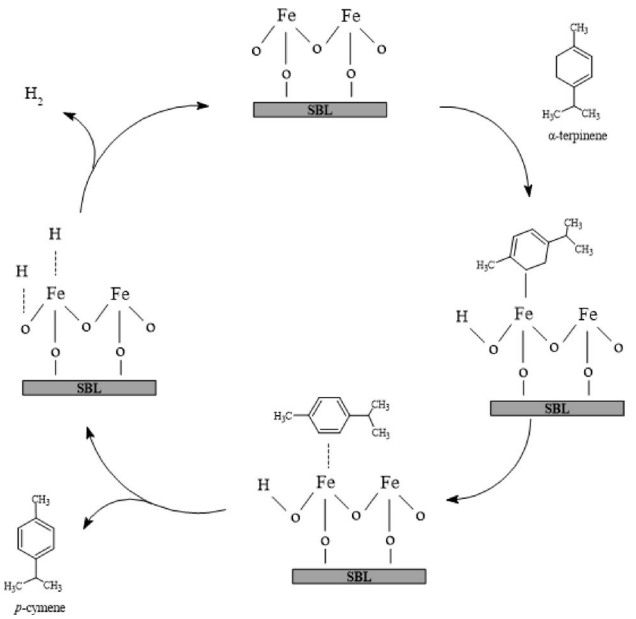

Fig. 16 Reaction pathway for the dehydrogenation step leading to *p*-cymene formation, based on [23]. Proposed scheme of the α-terpinene dehydrogenation mechanism for the formation of *p*-cymene on the LS600-HCl-Fe7% catalyst. The process occurs on Fe(III) sites of the supported iron oxide and involves the sequential abstraction of hydrogen and the subsequent formation and desorption of *p*-cymene. SBL corresponds to the sludge-based support, whose composition is mainly represented by the LS600-HCl material

LS600-HCl-Fe7% catalyst fulfills these criteria, as it exhibits strong Lewis acidity and a total acidity of 528.2 mmol NH_3 g^{-1}. In addition, it contains an active metallic phase in the form of hematite (Fe_2O_3), which provides Fe^{3+} sites. Based on these characteristics, the reaction pathway for the dehydrogenation of α-terpinene to *p*-cymene shown in Fig. 16 is proposed. It is plausible that the isomerization of limonene into other terpene intermediates occurs on the acidic sites located within the mesopores of the catalyst. Initially, the exocyclic double bond of limonene is protonated to form a primary carbenium ion, followed by proton shifts that stabilize the intermediate as tertiary carbenium ions, from which terpinolene and α-terpinene are generated [21] (Fig. 15, route I). Starting from α-terpinene, the dehydrogenation step is proposed to proceed through abstraction of an allylic hydrogen by an oxo-Fe(III) site, generating a surface-bound intermediate. Subsequent removal of a second hydrogen atom leads to the formation of *p*-cymene coordinated to the Fe(III) center through a π-interaction. Final desorption of *p*-cymene and release of H_2 closes the catalytic cycle (Fig. 16). This reaction pathway aligns with dehydrogenation mechanisms of hydrocarbons on metal oxide surfaces previously reported in the literature [23].

Table 7 Comparison of the catalytic performance of LS600-HCl and LS600-HCl-Fe7% with representative literature benchmarks for α-pinene isomerization to camphene and limonene transformation to *p*-cymene

Reagent	Product	Catalyst	T (°C)	t (h)	Mass (mg)	Solvent	Conversion (%)	Selectivity (%)	Reference
α-Pinene	Camphene	TiO_2	155	0.67	600	None	100	69	[7]
α-Pinene	Camphene	CLIN 0.1	70	0.06	2000	None	100	50	[8]
α-Pinene	Camphene	Ti-SBA-15	180	7	600	None	100	27	[10]
α-Pinene	Camphene	**LS600-HCl**	90	5	50	Cyclohexane	85	38	This work
Limonene	*p*-cymene	20% CdO/SiO_2	250	4	200	Gas phase	100	100	[23]
Limonene	*p*-cymene	Ti-MCM-41	170	24	750	None	96	46	[21]
Limonene	*p*-cymene	SIRAL 40	165	0.3	500	Microwave	100	100	[16]
Limonene	*p*-cymene	**LS600-HCl-Fe7%**	165	24	200	None	100	44	This work

A consolidated comparison of the catalytic performance of LS600-HCl and LS600-HCl-Fe7% with representative literature benchmarks is presented in Table 7. For α-pinene isomerization to camphene, LS600-HCl achieves 85% conversion and 38% selectivity at 90 °C with only 50 mg of catalyst, whereas TiO_2 [7] reaches 100% conversion and 69% selectivity but requires 155 °C and 600 mg of catalyst. For the limonene to *p*-cymene transformation, LS600-HCl-Fe7% achieves complete conversion and 44% selectivity at 165 °C with 200 mg of catalyst under neat conditions, whereas 20% CdO/SiO_2 [23] reaches 100% *p*-cymene selectivity but only under gas-phase conditions at 250 °C. Although our sludge-derived catalysts do not match the highest selectivities reported in the literature, they operate under significantly milder thermal conditions and with lower catalyst loadings, and are obtained from a low-cost, widely available waste stream underscoring their potential as sustainable catalytic alternatives.

4 Conclusions

Calcined and chemically treated sludges from a drinking water treatment plant proved to be viable precursors for the preparation of heterogeneous catalysts applicable to the transformation of monoterpenes. Acidification with HCl, particularly when combined with hydrothermal pretreatment, enhanced the catalytic properties of the sludge by generating Brønsted acid sites and reducing the aluminum content of the material, which in turn favored the relative enrichment of silica and the persistence of crystalline phases such as hematite that contribute to the catalytic behavior.

Metal impregnation with iron further modified the catalytic profile by increasing the contribution of Lewis acid sites and generating magnetite and maghemite phases. LS600-HCl exhibited appreciable selectivity toward camphene in the isomerization of α-pinene, attributable to the presence of Brønsted acid sites of moderate strength necessary to initiate the reaction. In contrast, LS600-HCl-Fe7% was selective toward *p*-cymene in the isomerization and dehydrogenation of limonene, consistent with its enhanced Lewis acidity and the presence of Fe^{3+} species capable of promoting the dehydrogenation step.

The reaction pathways proposed for both substrates indicate that p-cymene formation depends on the combined action of acidic and metallic sites, whereas excessive acidity favors the formation of high-molecular-weight species. Stability tests confirmed the heterogeneous nature of both catalysts and their capacity to be reused, with a gradual decrease in conversion but with stable selectivity toward the main products across cycles. Compared with several benchmark systems reported in the literature (Table 7), LS600-HCl-Fe7% reached complete limonene conversion and moderate *p*-cymene selectivity under significantly milder thermal conditions and with lower catalyst loadings, although with lower selectivity than the most optimized synthetic catalysts.

The influence of the reaction variables was assessed through two complementary statistical strategies: a full factorial design was applied to the isomerization of α-pinene over LS600-HCl in order to identify the main effects of catalyst amount, temperature, and reaction time on conversion within the studied range; whereas a central composite design was used for the transformation of limonene over LS600-HCl-Fe7% to model the response surfaces of conversion and *p*-cymene selectivity as a function of the same variables. These analyses provided a consistent description of the relative influence of the operating variables on the catalytic performance of each material.

Several limitations of the present study should be acknowledged in order to delimit the scope of these conclusions. First, iron dispersion on the catalyst surface was not directly measured, so the catalytic behavior of LS600-HCl-Fe7% should be interpreted as resulting from the combined effect of iron content, acid-site distribution, and mesoporous texture, rather than from a well-defined dispersion of the metal. Second, the comparison of the FTIR-Py spectra between fresh and reused catalyst is restricted to a qualitative interpretation, since the absolute band intensities depend on experimental variables (sample loading, ambient humidity)

that were not strictly controlled across measurements; this prevents a quantitative assessment of acid-site populations in the spent material, although the qualitative observation that the full set of pyridine bands is preserved supports the interpretation of deactivation by physical blocking of active sites rather than by chemical modification of the acid sites. Finally, the statistical analyses (factorial and central composite designs) describe the catalytic response within the operational ranges explored in this work and should not be extrapolated outside those ranges.

Overall, the combination of thermal and chemical treatments applied to the inorganic fraction of drinking water treatment sludge is shown here to be an effective strategy to obtain catalytically active materials for the transformation of α-pinene and limonene under mild operating conditions, and illustrates a potential valorization route for this industrial waste stream.

Supplementary Information The online version contains supplementary material available at https://doi.org/10.1007/s10562-026-05415-3.

Acknowledgements The authors gratefully acknowledge to Universidad de Antioquia (UdeA) for providing financial support for this research and EPM for supplying the sludge. M.M.G. thanks scholarship as Instructor Student from UdeA.

Author Contributions All authors reviewed the manuscript. Conceptualization and formal analysis: Mateo Moreno Giraldo and Aída Luz Villa. Methodology, Validation, Investigation, and Writing – original draft by Mateo Moreno Giraldo. Writing – review & editing, Supervision, Project administration, Funding acquisition: Aída Luz Villa. All authors read and approved the final manuscript.

Funding Open Access funding provided by Colombia Consortium. The authors gratefully acknowledge to Universidad de Antioquia (UdeA) for providing financial support for this research. M.M.G. thanks scholarship as Instructor Student from UdeA.

Data Availability The authors declare that the data supporting the findings of this study are available within the paper and its Supplementary Information files.

Declarations

Competing Interests The authors declare no competing interests.

References

1. Sanchis R et al (Mar. 2019) Ferric sludge derived from the process of water purification as an efficient catalyst and/or support for the removal of volatile organic compounds. Chemosphere 219:286–295. https://doi.org/10.1016/J.CHEMOSPHERE.2018.12.002
2. Mira R, Llano E (2018) Estudios de tratabilidad y deshidratación de lodos producidos en plantas de potabilización. Rev EPM 12:111
3. Liu Y et al (May 2021) The potential use of drinking water sludge ash as supplementary cementitious material in the manufacture of concrete blocks. Resour Conserv Recycl 168:105291. https://doi.org/10.1016/J.RESCONREC.2020.105291
4. Cheng F, Luo H, Hu L, Yu B, Luo Z, Cortalezzi MFD (Dec. 2016) Sludge carbonization and activation: From hazardous waste to functional materials for water treatment. J Environ Chem Eng 4(4):4574–4586. https://doi.org/10.1016/J.JECE.2016.11.013
5. Chiang KY et al (2013) Sep., Gasification of rice straw in an updraft gasifier using water purification sludge containing Fe/Mn as a catalyst, *Int. J. Hydrogen Energy*, vol. 38, no. 28, pp. 12318–12324. https://doi.org/10.1016/J.IJHYDENE.2013.07.041
6. Akgül M, özyağci B, Karabakan A (Jan. 2013) Evaluation of Fe- and Cr-containing clinoptilolite catalysts for the production of camphene from α-pinene. J Ind Eng Chem 19(1):240–249. https://doi.org/10.1016/J.JIEC.2012.07.024
7. Kumar S, Sinhmar PS, Gogate PR (Dec. 2021) Ultrasound assisted improved synthesis of TiO2 catalyst and subsequent evaluation for isomerization of alpha pinene. Chem Eng Process - Process Intensif 169:108591. https://doi.org/10.1016/J.CEP.2021.108591
8. Miądlicki P, Wróblewska A, Kiełbasa K, Koren ZC, Michalkiewicz B (Sep. 2021) Sulfuric acid modified clinoptilolite as a solid green catalyst for solvent-free α-pinene isomerization process. Microporous Mesoporous Mater 324:111266. https://doi.org/10.1016/J.MICROMESO.2021.111266
9. Rachwalik R, Góra-Marek K, Olejniczak Z, Hunger M, Sulikowski B (2020) Tailoring selectivity in the liquid-phase isomerization of α-pinene on dealuminated ferrierite-type zeolites, *Catal. Today*, vol. 354, pp. 141–150, Sep. https://doi.org/10.1016/J.CATTOD.2019.03.045
10. Wr Oblewska A, Mia ˛dlicki P, Sre Nscek-Nazzal J, Sadłowski M, Koren ZC, Michalkiewicz B (2017) Alpha-pinene isomerization over Ti-SBA-15 catalysts obtained by the direct method: The influence of titanium content, temperature, catalyst amount and reaction time, https://doi.org/10.1016/j.micromeso.2017.09.007
11. Sánchez-Velandia JE, Pájaro E, Villa AL, Martínez-O F (2021) Selective synthesis of camphene from isomerization of α-and β-pinene over heterogeneous catalysts, https://doi.org/10.1016/j.micromeso.2021.111273
12. Sinhmar PS, Gogate PR (May 2022) Improved Activation of Titanium Dioxide Catalyst for Isomerization of Alpha Pinene and Understanding into Effect of Isomerization Parameters. Arab J Sci Eng 47(5):5875–5893. https://doi.org/10.1007/S13369-021-05706-4/TABLES/4
13. Kamińska A, Sreńscek-Nazzal J, Serafin J, Miądlicki P, Kiełbasa K, Wróblewska A (2024) Biomass-based activated carbons produced by chemical activation with H3PO4 as catalysts for the transformation of α-pinene to high-added chemicals, *Environ. Sci. Pollut. Res.*, vol. 31, no. 28, pp. 40063–40082, Jun. https://doi.org/10.1007/S11356-023-28232-2
14. Brazovskaya EY et al (2025) Apr., Preparation, Acidity, and Catalytic Activity of Synthetic Montmorillonites in α-Pinene

Isomerization, *Langmuir*, vol. 41, no. 15, pp. 9631–9644. https://doi.org/10.1021/ACS.LANGMUIR.4C04825
15. Lv T, Wei K, Wang T, Wang X, Liu Z (Jan. 2025) Synergistic catalysis for converting α-pinene to camphene via carbon-based solid acid derived from eucalyptus wood. Mol Catal 571:114717. https://doi.org/10.1016/j.mcat.2024.114717
16. Martín-Luengo MA et al (2008) Jun., Synthesis of *p*-cymene from limonene, a renewable feedstock, *Appl. Catal. B Environ.*, vol. 81, no. 3–4, pp. 218–224. https://doi.org/10.1016/J.APCATB.2007.12.003
17. Lycourghiotis S, Makarouni D, Kordouli E, Bourikas K, Kordulis C, Dourtoglou V (2018) Activation of natural mordenite by various acids: Characterization and evaluation in the transformation of limonene into *p*-cymene. Mol Catal. https://doi.org/10.1016/j.mcat.2018.03.013
18. Yılmazoğlu E, Akgün M (Jan. 2018) -Cymene production from orange peel oil using some metal catalyst in supercritical alcohols. J Supercrit Fluids 131:37–46. https://doi.org/10.1016/J.SUPFLU.2017.08.015
19. Martin-Luengo MA, Yates M, Rojo ES, Huerta Arribas D, Aguilar D, Ruiz Hitzky E (2010) Sustainable *p*-cymene and hydrogen from limonene, *Appl. Catal. A Gen.*, vol. 387, no. 1–2, pp. 141–146, Oct. https://doi.org/10.1016/J.APCATA.2010.08.016
20. Lycourghiotis S, Makarouni D, Kordouli E, Bourikas K, Kordulis C, Dourtoglou V (2020) Transformation of limonene into high added value products over acid activated natural montmorillonite, *Catal. Today*, vol. 355, pp. 757–767, Sep. https://doi.org/10.1016/J.CATTOD.2019.04.036
21. Retajczyk M, Wróblewska A (Jun. 2019) Isomerization and Dehydroaromatization of R(+)-Limonene Over the Ti-MCM-41 Catalyst: Effect of Temperature, Reaction Time and Catalyst Content on Product Yield. Catal 2019 9(6):508. https://doi.org/10.3390/CATAL9060508
22. Tavera Ruiz CP et al (2018) Transformation of dl Limonene into Aromatic Compounds Using Supported Heteropolyacid Catalysts. Catal Lett 1491(149, 1):328–337. https://doi.org/10.1007/S10562-018-2606-Y. Nov. 2018
23. Alsharif A, Kozhevnikova EF, Kozhevnikov IV (May 2023) Selective dehydroisomerization of cyclic monoterpenes to *p*-cymene over silica-supported CdO. Appl Catal B Environ 325:122362. https://doi.org/10.1016/J.APCATB.2023.122362
24. Kaya B, Zengin Y, Boroglu MS, Boz I (2022) Selective dehydration of glycerol to acrolein over mesoporous WO3-KIT-6: effects of mesoporosity and acidity, *J. Porous Mater.* vol. 30, no. 3, pp. 835–845, Nov. 2022. https://doi.org/10.1007/S10934-022-01384-1
25. Iverson BL, Dervan PB (2015) Estudio de las variables de operación del proceso de pirólisis catalítica de polietileno, pp. 7823–7830
26. Fierro G, Moretti G, Ferraris G, Andreozzi GB (2011) A Mössbauer and structural investigation of Fe-ZSM-5 catalysts: Influence of Fe oxide nanoparticles size on the catalytic behaviour for the NO-SCR by C3H8, *Appl. Catal. B Environ.*, vol. 102, no. 1–2, pp. 215–223, Feb. https://doi.org/10.1016/J.APCATB.2010.12.001
27. Salgado-Ramos M, Tabasso S, Gaudino EC, Cravotto G (May 2024) Process Intensification for Sustainable Microwave-Assisted Bio *p*-Cymene Production from Limonene. Ind Eng Chem Res 63:7507–7518. https://doi.org/10.1021/ACS.IECR.4C00117
28. Makarouni D, Lycourghiotis S, Kordouli E, Bourikas K, Kordulis C, Dourtoglou V (May 2018) Transformation of limonene into *p*-cymene over acid activated natural mordenite utilizing atmospheric oxygen as a green oxidant: A novel mechanism. Appl Catal B Environ 224:740–750. https://doi.org/10.1016/J.APCATB.2017.11.006